AD-A088 122 CALIFORNIA UNIV BERKELEY ELECTRONICS RESEARCH LAB F/G 20/9
PLASMA THEORY AND SIMULATION.(U)
SEP 79 C K BIRDSALL, A FRIEDMAN, W FAWLEY N00014-77-C-0578

UNCLASSIFIED NL

1 OF 2
AD A088122

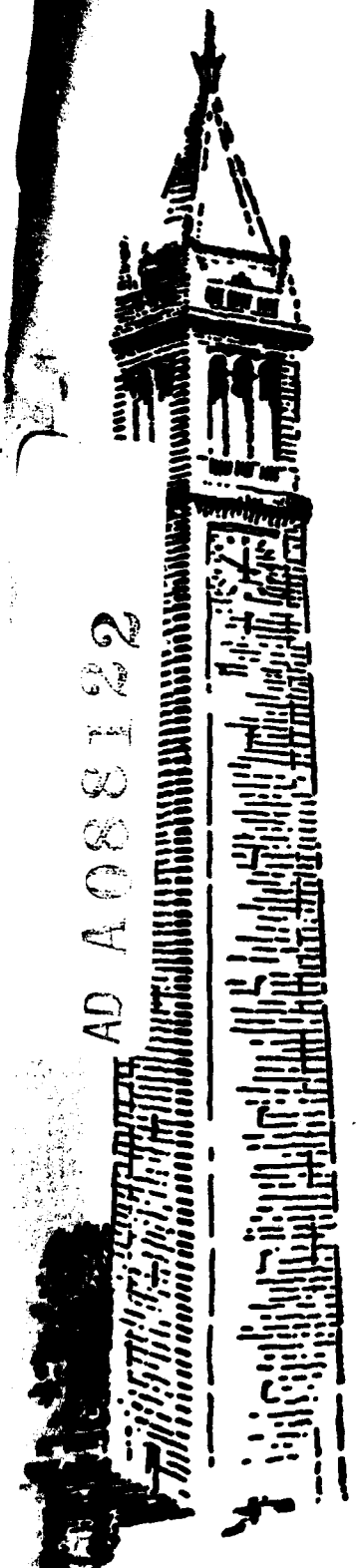

AD A088182

DDC FILE COPY

LEVEL II

12

A065157

THIRD QUARTER PROGRESS REPORT ON

PLASMA THEORY AND SIMULATION

DTIC ELECTE AUG 12 1980 S C D

July 1 - September 30, 1979

DOE Contract DE-AS03-76F00034-DE-AT03-76ET53064
ONR Contract N00014-77-C-0578

This document has been approved for public release and sale; its distribution is unlimited.

ELECTRONICS RESEARCH LABORATORY
College of Engineering
University of California, Berkeley, CA 94720

80 4 10 007

THIRD QUARTER PROGRESS REPORT

PLASMA THEORY and SIMULATION

(July 1 to Sept 30, 1979)

Research during the Third Quarter of 1979 is reported here.

Our research group uses both theory and simulation as tools in order to increase the understanding of instabilities, heating, transport, and other phenomena in plasmas. We also work on the improvement of simulation, both theoretically and practically.

Our staff is (10)

Professor C. K. Birdsall *Principal Investigator*	191 M	Cory Hall	(642-4015)
Alex Friedman & William Fawley *Post Doctorates*	119 ME	Cory Hall	(642-3477)
Yu Jiuan Chen & Douglas Harned, Vincent Thomas, Niels Otani *Research Assistants*	119 MD	Cory Hall	(642-1297)
Stephen Au-Yeung *Programmer*	119 MD	Cory Hall	(642-1297)
Mike Hoagland *Research Typist*	199 M	Cory Hall	(642-7919)

Sept 30, 1979

DOE Contract DE-AS03-76F00034-DE-AT03-76ET53064
ONR Contract N00014-77-C-0578

ELECTRONICS RESEARCH LABORATORY

College of Engineering
University of California, Berkeley
94720

This document has been approved for public sale; its distribution is unlimited.

TABLE OF CONTENTS

Section I

PLASMA THEORY and SIMULATION

A.	Filamentation in Charged Particle Beams	1
B.	Drift-Cyclotron Instability Particle Simulations	1
C.*	Lower Hybrid Drift Instability Simulations Using ES1 Hybrid Code	1
D.*	Nonlinear Perturbation Theory of the Lower Hybrid Drift Instability	14
E.*	Control of Unwanted Beaming Instabilities	27
F.	Transverse Oscillations of a Current Sheet in a Plasma — Theory	28
G.*	Transverse Oscillations of a Current Sheet in a Plasma — Simulation	36
H.*	Field Reversed Plasma Simulations, Quasineutral, in 2d	42
I.	Field Reversed Plasma Stability; Linearized Hybrid Simulations in 3d	51
J.	Pulsar Sparking	57
K.	Digital Filtering in Time	57
L.	Nonphysical Behavior of Hybrid Oscillations Due to Aliasing	59

Section II

CODE DEVELOPMENT and MAINTENANCE

A.	ES1 Code	71
B.	EM1 Code	71
C.	EZOHAR Code	71
D.	ES1 + EFL Code	71
E.	RINGHYBRID Code	71
F.	Radial Simulation Code ES1RB	72
G.	Condition on Particle Shapes in 1d Radial Codes	82
H.	Radial Code Notes (R,Rθ,RZ, RθZ)	85
I.	RJET Development	95
J.	Software Developments (FREX,COMOUT,DB,TIME)	96
K.	Report Generation	104

Section III

PLASMA SIMULATION TEXT 106

Section IV

SUMMARY of REPORTS TALKS and PUBLICATIONS in the PAST QUARTER 106

Distribution List 108

*Indicates ONR supported areas.

Section I
PLASMA THEORY and SIMULATION

A. FILAMENTATION IN CHARGED PARTICLE BEAMS

Lee Buchanan has transferred to LLL where this work will continue. No further report.

B. DRIFT-CYCLOTRON INSTABILITY PARTICLE SIMULATIONS

Jae Koo Lee (Prof. C. K. Birdsall)

Work continuing on the final report. No further report.

C. LOWER HYBRID DRIFT INSTABILITY SIMULATIONS USING ES1 HYBRID CODE

Yu-Jiuan Chen (Dr. B. I. Cohen (LLL) and Prof. C. K. Birdsall)

The linear properties of the lower-hybrid drift instability were studied using a 1d particle-hybrid simulation, as shown in the last QPR. The model is a slab with a constant density gradient; the ions are unmagnetized particles, shielded by the strongly magnetized electrons through the linear electron susceptibility, χ_e. Ions are initially in a steady equilibrium state with the ion diamagnetic drift velocity cancelled by the $\underline{E} \times \underline{B}$ drift, corresponding to electrostatically confined ions.

The saturation mechanisms of the instability are studied. In the last QPR, Fig. 5 shows the complex frequency versus v_E/v_{ti} for $\omega_{pe}^2/\omega_{ce}^2 = 1$, $m_i/m_e = 1600$, $T_e = 0$, $L_n/L_B = 0$, $L_n/L_T = 0$, and the mode number $m = 5$ (i.e., $k\lambda_D = 1/\sqrt{2}$), which is approximately the most unstable mode for the parameters we used. v_E is the $\underline{E} \times \underline{B}$ drift velocity, v_{ti} is defined as $\sqrt{T_i/m_i}$, and L_n, L_B and L_T are the scale lengths of the density, magnetic field and temperature, respectively. Since the growth rate γ is comparable to the wave frequency,

the mode has a wide band width $\Delta\omega \sim \gamma$; and thus quasilinear diffusion is one of the possible mechanisms for the saturation of such modes. Allowing only a single mode, we compared the saturation levels of mode 5 with the quasilinear theory as given by R. C. Davidson (Refs. 1 and 2) under assumption that the spectrum is strongly peaked about the fastest growing mode, for $v_E < v_{ti}$. Figs. 1 and 2 show that the simulation data are in agreement with the quasilinear saturation level ε_s in Eq. 48*

$$\varepsilon_s = \frac{2}{45\sqrt{\pi}} \left(\frac{v_E}{\sqrt{2}v_{ti}}\right)^5 \frac{NT_i}{1 + \omega_{pe}^2/\omega_{ce}^2} \quad , \tag{1}$$

where N is the number of ions. However, it is found from the evidence of oscillations of the wave energy at the trapping frequency ω_T (Figs. 2a and 2b) and the vortex-like structure in the ion phase space plots after saturation (Figs. 3a and 3b) for $v_E/v_{ti} = 0.57$ and 0.85 that the end of wave growth was accomplished by ion trapping. All of the phase space pictures are presented in the wave frame, $x - v_{ph}$ = constant, where v_{ph} was calculated from linear theory. It is noted that vortices in Figs. 3a and 3b at small velocities are not due to the multibeam instability, because those vortices would appear at large velocities.

Our explanation of why the simulations showed that nonlinear saturation was due to ion trapping but saturation levels agreed with the quasilinear theory is as follows. In deriving the saturation level ε_s (Eq. 1), Davidson began with an energy conservation equation and the only rea invocation of quasilinear theory seems to be the specification that saturation occurs when the distribution function has been "flattened" around the mode

*In all of Davidson's equations, there is a factor of $\sqrt{2}$ difference in v_{ti} due to his definition of $T_i = m_i v_{ti}^2/2$.

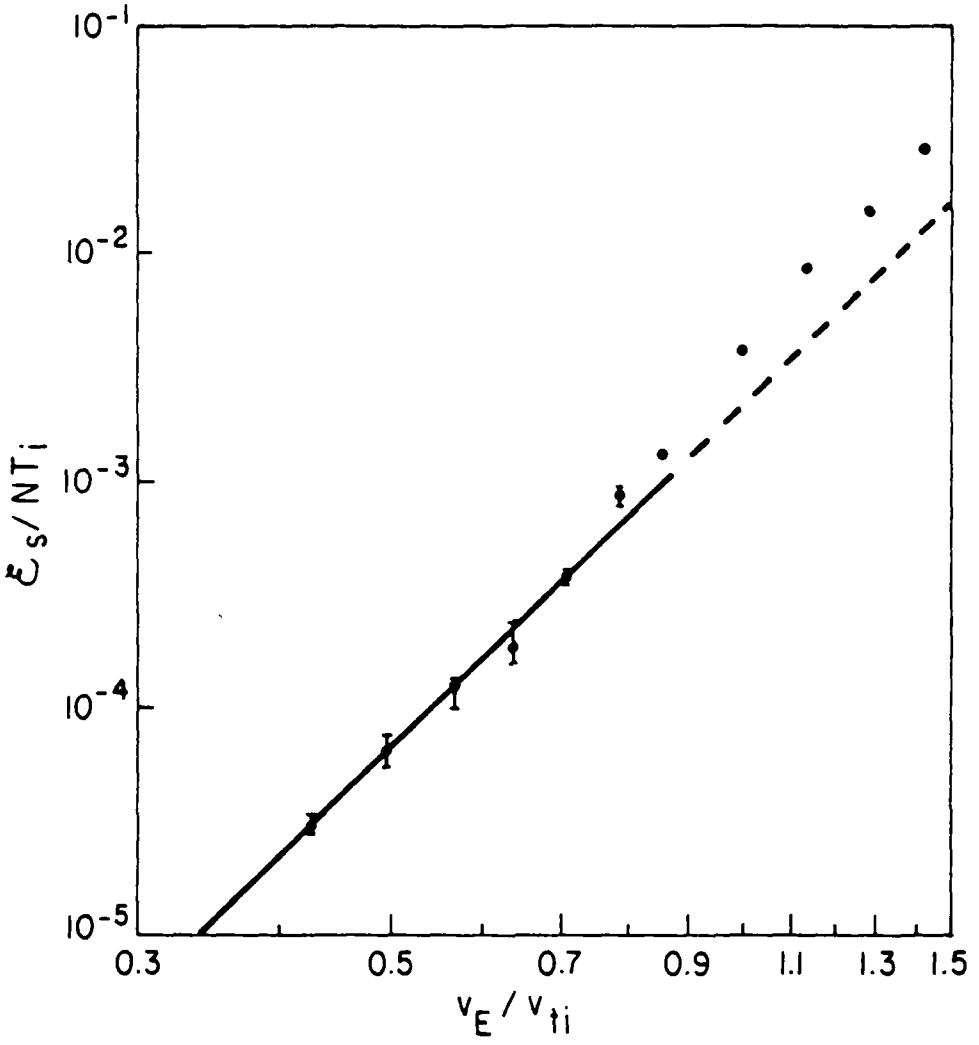

FIG. 1 Saturation field energy for the most unstable LHDI mode as function of v_E/v_{ti}. The simulation data (dots) are in agreement with the theory shown by lines as discussed in the text.

Accession For
NTIS GRA&I
DTIC TAB
Unannounced
Justification
By
Distribution/
Availability Codes
Dist | Avail and/or special
A

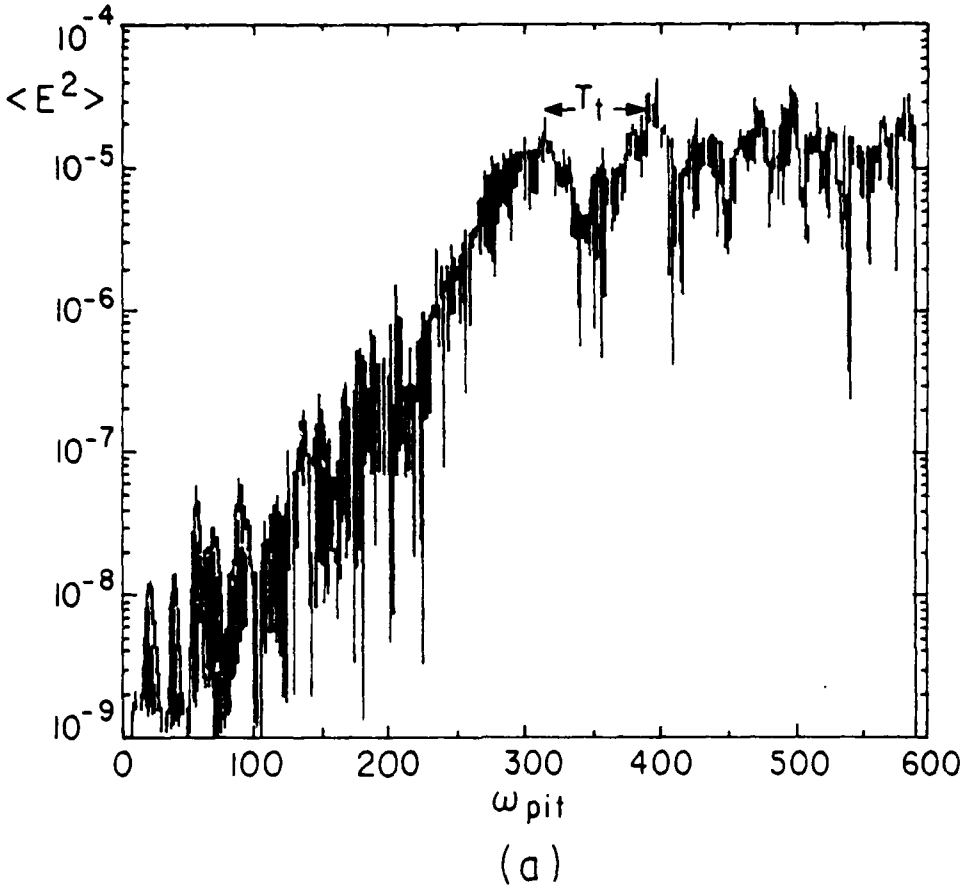

FIG. 2 Electric field energy history plots for $m_i/m_e = 1600.$, $\omega_{pe}^2/\omega_{ce}^2 = 1.$, $T_e = 0.$, $k\lambda_D = 1/\sqrt{2}.$, $L_n/L_B = 0.$, $L_n/L_T = 0.$, (a) $v_E/v_{ti} = 0.57$; the high frequencies are due to the multibeam instability and low frequencies are due to the LHDI; the growth is that of LHDI as discussed in previous QPR's (using ω spectrum), and (b) $v_E/v_{ti} = 0.85$; the multibeaming effect is very small (next page).

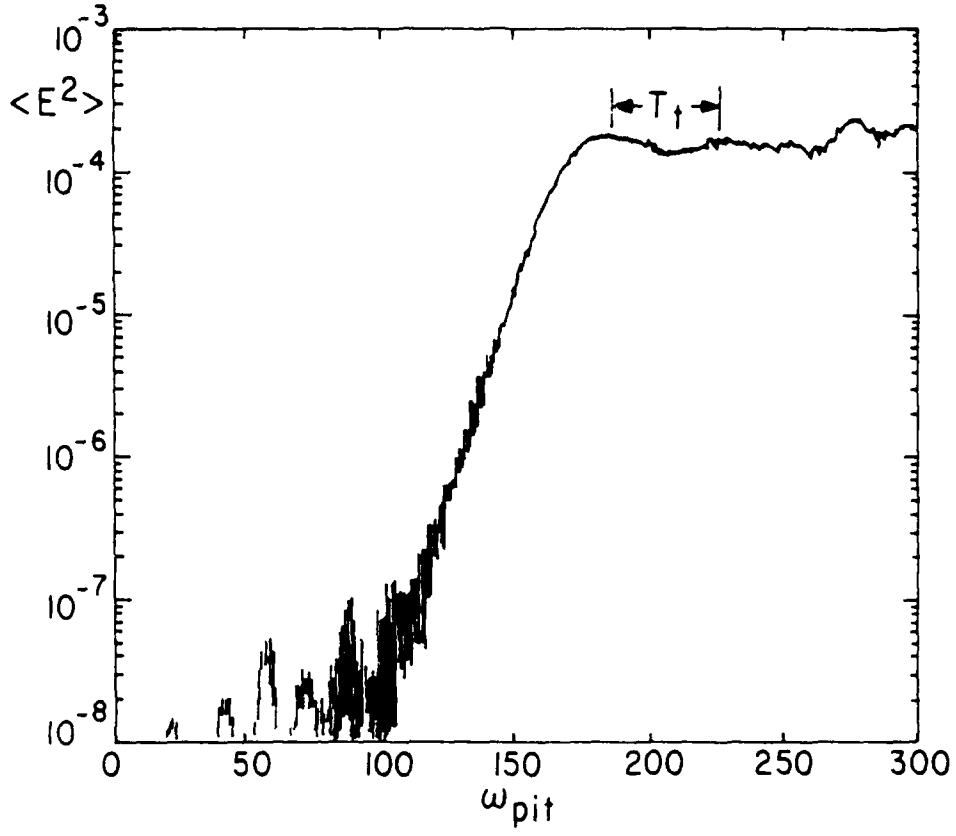

(b)

FIG. 2(b)

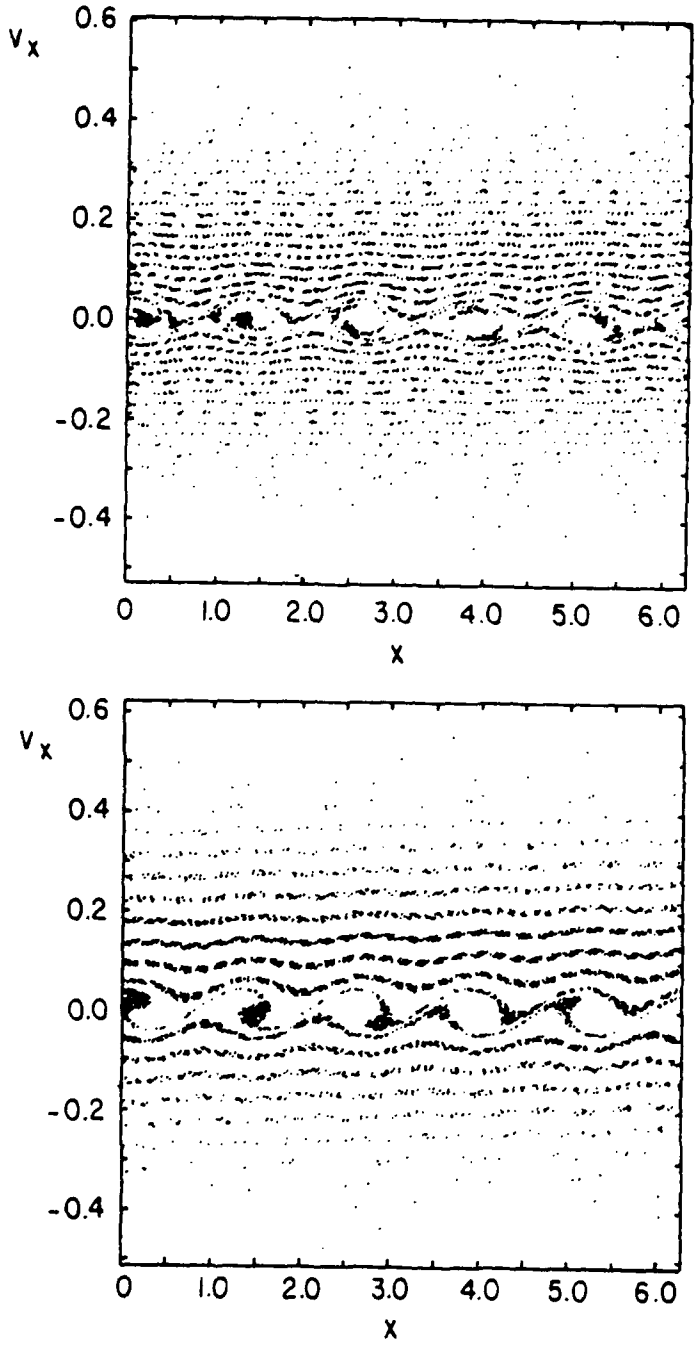

FIG. 3 Ion phase space pictures in the LHDI wave frames after saturation for $m_i/m_e=1600.$, $\omega_{pe}^2/\omega_{ce}^2=1.$, $T_e=0.$, $k\lambda_D=1/\sqrt{2}.$, $L_n/L_B=0.$, $L_n/L_T=0$, (a) $v_E/v_{ti}=0.57$, and (b) $v_E/v_{ti}=0.85$. The dots were plotted one of every 5 points.

phase velocity. Such flattening could in principle be due to a variety of causes besides the usual quasilinear diffusion, for example, trapping. Furthermore, the trapping frequency is given by

$$\omega_T = k_m \sqrt{\frac{e\phi}{m_i}} , \tag{2}$$

where

$$\phi = \sqrt{\frac{8\pi\varepsilon_s}{k_m^2 V}}$$

is the electric potential, and k_m is the wave number of the most unstable mode. From Eq. 1, we obtain

$$\omega_T = (k_m v_{ti} \omega_{\ell h})^{\frac{1}{2}} \left(\frac{2}{45\sqrt{\pi}}\right)^{\frac{1}{4}} \left(\frac{v_E}{\sqrt{2} v_{ti}}\right)^{5/4} , \tag{3}$$

where

$$\omega_{\ell h} = \frac{\omega_{pi}}{\sqrt{1 + \omega_{pe}^2/\omega_{ce}^2}}$$

is the lower hybrid frequency. From Ref. 1, the corresponding growth rate and wave number at maximum growth are expressed by

$$\gamma_m = \frac{\sqrt{2\pi}}{8} \left(\frac{v_E}{\sqrt{2} v_{ti}}\right)^2 \omega_{\ell h} , \tag{4}$$

$$k_m = \omega_{\ell h}/v_{ti} . \tag{5}$$

Therefore, Eq. 3 can be rewritten as

$$\frac{\omega_T}{\gamma_m} = \left(\frac{2}{45\sqrt{\pi}}\right)^{\frac{1}{4}} \frac{8}{\sqrt{2\pi}} \left(\frac{\sqrt{2}v_{ti}}{v_E}\right)^{3/4}$$

$$= 1.647 \left(\frac{v_{ti}}{v_E}\right)^{3/4}. \qquad (6)$$

When $v_E < v_{ti}$, the trapping frequency is larger than the growth rate and hence the bandwidth $\Delta\omega$ as well; and the ion trapping will be the saturation mechanism whenever the fastest growing mode is dominant. Then ε_s in Eq. 1 is the saturation level due to ion trapping. Comparison of Eq. 6 with the observed trapping frequencies (as in Fig. 4) indicates fairly good agreement for cases in which $v_E \leq v_{ti}$.

An estimate of the fluctuation energy at saturation may be made through the use of the Fowler thermodynamic bound (Ref. 3); one possible form of this bound on the saturation level can be obtained by assuming that the system stabilizes via current relaxation (meaning $v_E \to 0$) as v_E drives the instability. However, this bound is not applicable in our simulations as our model has assumed a constant density gradient and v_E drift.

Finally, multimode simulations have been done, i.e., all the modes are excited at the initial stage. Typical parameters are the same as those for the single mode run, which were given in the last QPR. The fastest growing mode tended to reach the same saturation level no matter whether only a single mode was kept or all modes were included in the simulations. In the frame of the most unstable mode, the ion phase space plot reveals a vortex formation about $v_x = 0$ after saturation for $v_E/v_{ti} = 0.57$ as shown in Fig. 5a. The length of the plasma $L = 2\pi$, and the number of grids $NG = 64$. Also a dip appears at the approximate wave phase velocity

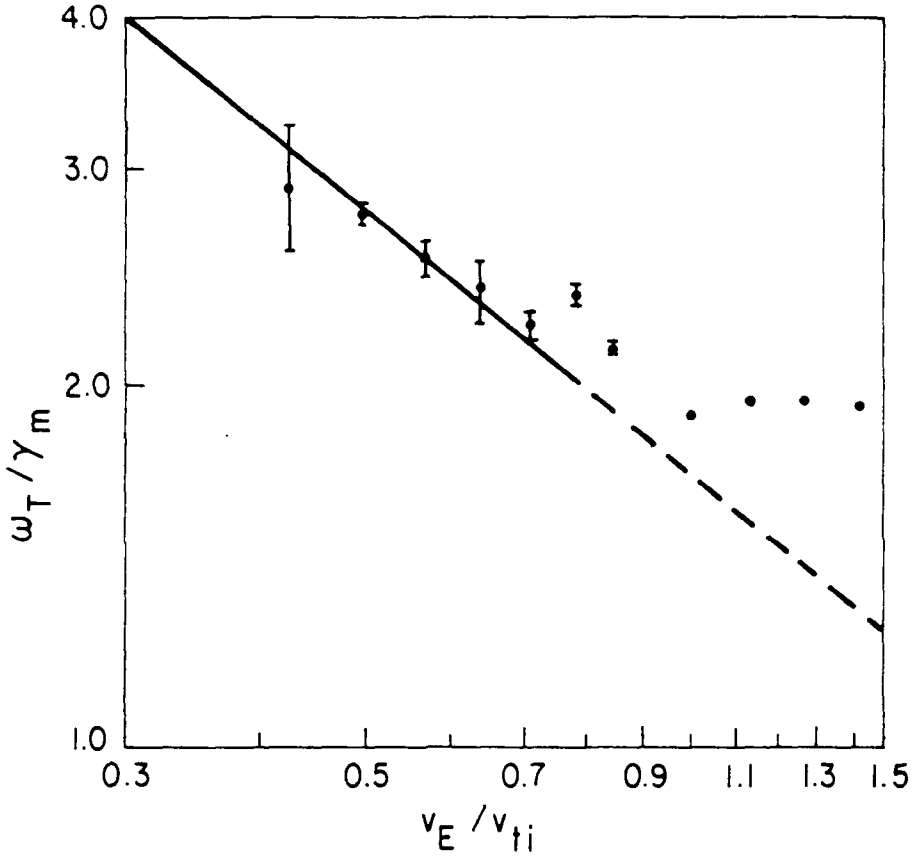

FIG. 4 Comparison of 1d simulation data (single mode) with the theory:

$$\frac{\omega_T}{\gamma_{max}} = 1.647 \left(\frac{v_{ti}}{v_E} \right)^{3/4} \qquad \text{(Eq. 6)}$$

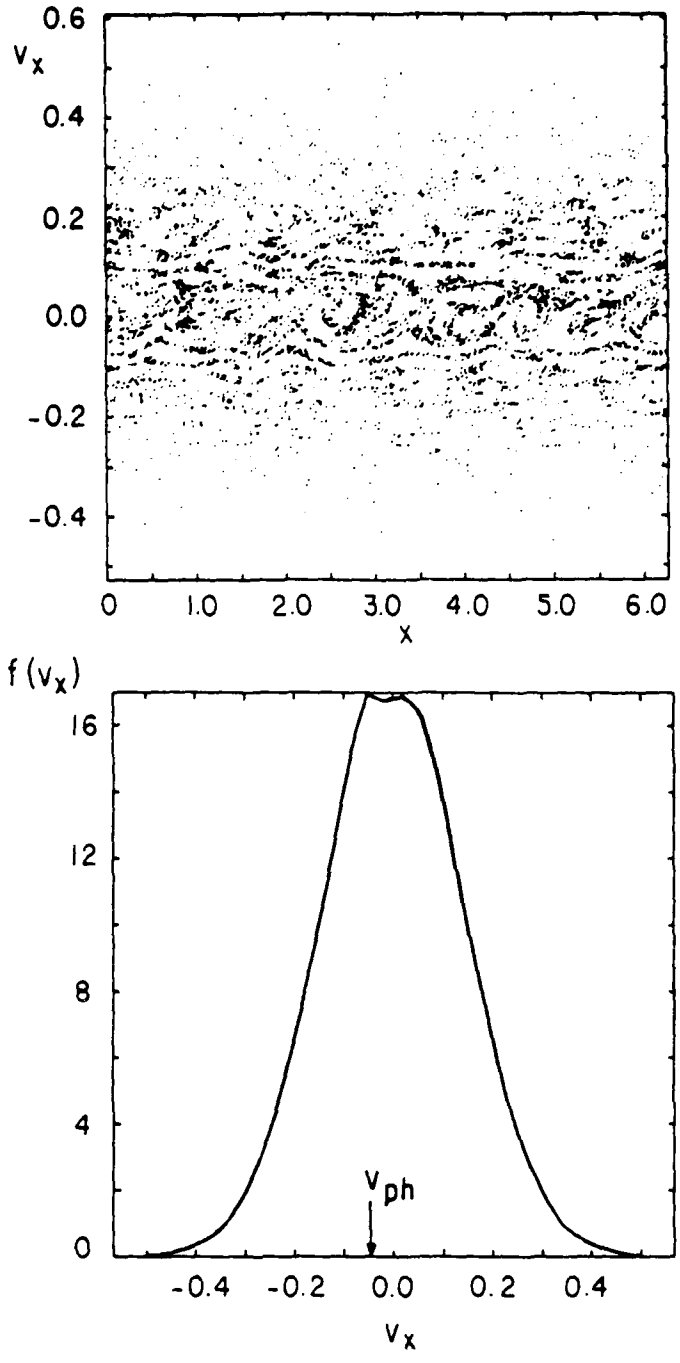

FIG. 5 Simulation (many mode) of LHDI with N = 16384, $\omega_{pe}^2/\omega_{ce}^2 = 1.$, $m_i/m_e = 1600.$, $v_E/v_{ti} = 0.57$, $T_e = 0.$, $L_n/L_B = 0.$, $L_n/L_t = 0.$, $\lambda_D/\Delta x = 0.1414$. Displayed are (a) the phase space in the most unstable mode frame, and (b) the ion velocity distribution function after satuation. v_{ph} is the wave phase velocity.

in the ion distribution curve in Fig. 5b. As $v_E/v_{ti} = 0.85$, the ion phase space and the distribution curve are presented in Figs. 6a and 6b for $L = 2\pi$ and $NG = 64$. The corresponding ion phase space picture for $L = 4\pi$, and $NG = 128$ is given in Fig. 7. It shows that trapping still occurred for a finer mode spacing, viz. when Δk was reduced to half, i.e., $\Delta k\lambda_D = 0.07$. Figs. 5, 6 and 7 show the dominant mode at saturation to be $\lambda_D \sim 1/\sqrt{2}$, which is the fastest growing mode.

Our simulations exhibited strong ion trapping at saturation in all cases in the low-drift-velocity regime with $v_E < v_{ti}$. These results do not necessarily rule out quasilinear diffusion as a possible cause for saturation as the simulations had discrete modes (not a continuous wave-number spectrum); however, as each mode has a large frequency bandwidth (due to large γ), auto-correlation time of the electric field is significantly reduced. Trapping was also obtained by D. Winske and P. C. Liewer (Ref. 4) in their 2d particle simulations with v_E larger than v_{ti}.

REFERENCES

1. R. C. Davidson, "Quasilinear Stabilization of Lower-Hybrid Drift Instability", Phys. Fluids 21, 1375 (1978).
2. R. C. Davidson and N. T. Gladd, "Anomalous Transport Properties Associated with the Lower-Hybrid Drift Instability", Phys. Fluids 18, 1327 (1975).
3. T. K. Fowler, in "Advances in Plasma Physics", edited by A. Simon and W. B. Thompson (Wiley, New York, 1968), Vol. 1, p. 201.
4. D. Winske and P. C. Liewer, "Particle Simulation Studies of the Lower Hybrid Drift Instability", Phys. Fluids 21, 1017 (1978).

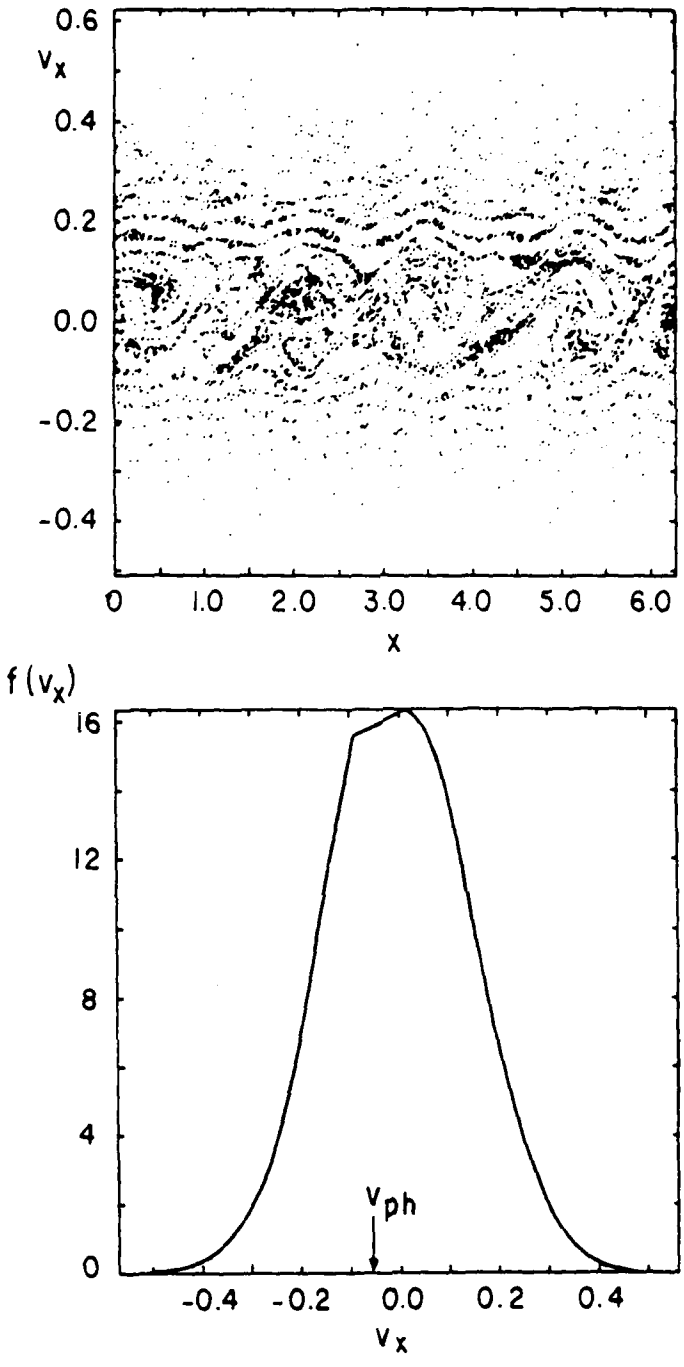

FIG. 6 Simulation (many mode) of LHDI with $N = 16384$, $\omega_{pe}^2/\omega_{ce}^2 = 1.$, $m_i/m_e = 1600.$, $T_e = 0.$, $v_E/v_{ti} = 0.85$, $L_n/L_B = 0.$, $L_n/L_T = 0.$, $\lambda_D/\Delta x = 0.1414$. Displayed are (a) the phase space in the most unstable mode frame, and (b) the ion velocity distribution function after saturation. v_{ph} is the wave phase velocity.

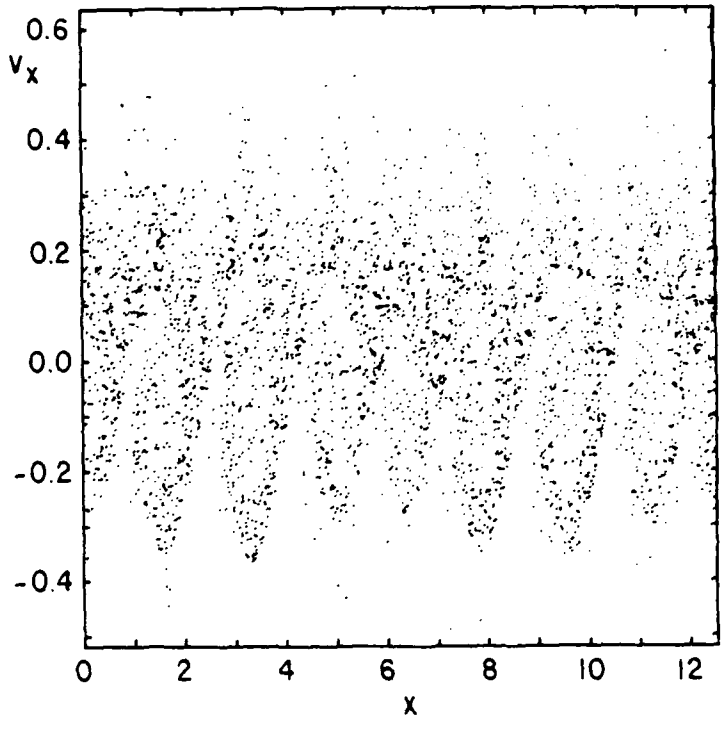

FIG. 7 The ion phase space in the most unstable mode frame after the saturation as N = 16384. $\omega_{pe}^2/\omega_{ce}^2 = 1.$, $m_i/m_e = 1600$, $v_E/v_{ti} = 0.85$, $T_e = 0.$, $L_n/L_B = 0.$, $L_n/L_T = 0.$, $\lambda_D/\Delta x = 1.44$, and $\Delta k\lambda_D = 0.0707$ (i.e., Δk half that of Fig. 6, but L twice that, so the dominant mode seen is the same).

D. NONLINEAR PERTURBATION THEORY OF THE LOWER-HYBRID DRIFT INSTABILITY

Yu-Jiuan Chen (Dr. B. I. Cohen and Prof. C. K. Birdsall)

The linear theory of the lower-hybrid drift instability is well understood and has been discussed in detail by Davidson et al. (Ref. 1). When the amplitude of the wave is small but finite after a time of the order of the inverse growth rate, its further evolution will be different from the linear exponential growth. The nonlinear dielectric response function and an analysis of the nonlinear time evolution of a single unstable mode are derived self-consistently by using perturbation theory to solve the Vlasov equation and the Poisson equation. The single-mode approximation is valid for the instability close to the stability limit which requires $v_E \ll v_{ti}$ (the low drift velocity regime) for the lower hybrid drift instability. Modulation of the Langmuir wave due to the nonlinearity has been investigated extensively in the single-mode approximation (Refs. 2 and 3). The nonlinear evolution of drift-cyclotron and drift-cone instabilities for plasmas very close to linear marginal stability have been studied in detail in both theory (Refs. 4, 5, 6 and 7) and simulation (Ref. 8).

For simplicity, we use a one-dimensional slab configuration with wave propagation in the x direction, uniform magnetic field in the z direction, and the density gradient in the y direction. The ions are unmagnetized as the wave frequency and growth rate are much greater than the ion cyclotron frequency, and electrostatically confined with the ion diamagnetic drift cancelled by the $\underline{E} \times \underline{B}$ drift, v_E.

In Sect. II, the nonlinear dielectric function is introduced by solving the coupled Vlasov-Poisson equations. Sect. III is devoted to dereive the time evolution of the lower-hybrid drift instability. The nonlin-

ear dispersion relation obtained is used to determine the field energy level and the frequency shift due to the finite amplitude of the wave. Finally, our conclusions are given in Sect. IV.

II. Derivation of Nonlinear Dielectric Function

According to the general theory of the reductive perturbation method, we assume that the distribution functions $F(y,\underline{v},t)$ and the electric potential $\phi(x,t)$ can be expanded as

$$F^s(y,\underline{v},t) = \tilde{F}^s_o(y,\underline{v}) + \sum_{n=1}^{\infty} \varepsilon^n \tilde{F}^s_n(y,\underline{v},t)e^{in\theta} + c.c. \tag{1}$$

and

$$\phi(x,t) = \sum_{n=1}^{\infty} \varepsilon^n \tilde{\phi}_n(x,t)e^{in\theta} + c.c. \tag{2}$$

where

$$\tilde{F}^s_n(y,\underline{v},t) = \sum_{j=0}^{\infty} \varepsilon^j F^s_{nj}(y,\underline{v},t) \quad , \quad n = 0,1,\ldots \tag{3}$$

$$\tilde{\phi}_n(x,t) = \sum_{j=0}^{\infty} \varepsilon^j \phi_{nj}(x,t) \quad , \quad n = 1,2,\ldots \tag{4}$$

$$\theta \equiv kx - \omega t \tag{5}$$

and $\varepsilon = \mathcal{O}(e\phi/T_i) \ll 1$. T_i is the ion temperature, and k and ω are the wave number and frequency of a single mode. Quasilinear analysis indicates the current relaxation causes saturation for $v_E < v_{ti}$ (Ref. 9), where $v_{ti}^2 = T_i/M$ is the ion thermal speed. However, the effect of the current relaxation is

small for $v_E \ll v_{ti}$. Therefore, the density gradient and v_E are kept constant in our derivation. The distribution function $F_{nj}(y,\underline{v},t)$ can be expressed as

$$F_{nj}(y,\underline{v},t) = n_o(y) f_{nj}(\underline{v},t) \ . \tag{6}$$

The Poisson equation of the system is

$$-\nabla^2\phi = 4\pi n_o e \int d\underline{v} \ (f^i - f^e) \ . \tag{7}$$

Substituting Eqs. (1) and (2) into Eq. (6) yields

$$(nk)^2\tilde{\phi}_n = 4\pi n_o e \int d\underline{v} \ (\tilde{f}^i_n - \tilde{f}^e_n) \ . \tag{8}$$

Since the characteristic frequency of the lower-hybrid drift instability is much less than the electron plasma and cyclotron frequencies, it is assumed that electrons respond to the wave linearly, i.e.,

$$-4\pi n_o e \int d\underline{v} \ \tilde{f}^e_n = -\chi_e(nk,n\omega)(nk)^2\tilde{\phi}_n \tag{9}$$

where χ_e is the electron linear susceptibility. We also assume a zero plasma beta value ($T_e \to 0$) to neglect electron resonance broadening which can stabilize the instability (Ref. 10). Using Eqs. (3), (4), and (9), Eq. (8) reduces to

$$[1 + \chi_e(nk,n\omega)](nk)^2\phi_{nj} = 4\pi n_o e \int f^i_{nj} \ d\underline{v} \ . \tag{10}$$

The one-dimensional Vlasov equation for the ion distribution is

$$\frac{\partial F^i}{\partial t} + v\frac{\partial F^i}{\partial x} - \frac{e}{M}\frac{\partial \phi}{\partial x}\frac{\partial F^i}{\partial v} = 0 \ , \tag{11}$$

where M is the ion mass. Since the density is varied in the y direction only, i.e., $\partial F^i/\partial x = 0$, Eq. (11) is rewritten as

$$\frac{\partial f^i}{\partial t} = \frac{e}{M}\frac{\partial \phi}{\partial x}\frac{\partial f^i}{\partial v} \quad . \tag{12}$$

With the assumption of a small perturbation, the above equation can be integrated over the unperturbed orbits, i.e.,

$$f^i - f^i_{oo} = \frac{e}{M}\int_{-\infty}^{t}\frac{\partial \phi}{\partial x}\frac{\partial f^i}{\partial v}\,dt' \quad . \tag{13}$$

or

$$\sum_{j=1}^{\infty}\varepsilon^j\left[f_{oj} + \sum_{n=1}^{j}\left(f_{n,j-n}e^{in\theta} + c.c.\right)\right]$$

$$= \sum_{j=1}^{\infty}\varepsilon^j\frac{e}{M}\int_{-\infty}^{t}\sum_{\substack{n=1\\ \ell=0}}^{\infty}\left\{\left(ink\phi_{n\ell}e^{in\theta'} + c.c.\right)\right.$$

$$\left.\cdot\left[\frac{\partial f_{o,j-n-\ell}}{\partial v} + \sum_{n'=1}^{\ell}\left(\frac{\partial f_{n',j-n-\ell-n'}}{\partial v}e^{in'\theta'} + c.c.\right)\right]\right\}dt' \quad . \tag{14}$$

Note that ion trapping is excluded under this assumption. The superscript i is dropped from Eq. (14). For j=1, comparing the coefficients of exp(inθ) of Eq. (14) yields

$$f_{01} = 0 \quad , \tag{15}$$

and

$$f_{10} = \frac{e\phi_{10}}{M} \cdot \frac{\partial f_{oo}/\partial v}{v - V} \tag{16}$$

where $V \equiv \omega/k$. Substituting Eq. (16) into Eq. (10), then we obtain

$$\left[1 + \chi_e(k,\omega)\right] k^2 \phi_{10} = \frac{4\pi n_o e^2}{M} \phi_{10} \int_o \frac{\partial f_{oo}/\partial v}{v - V} dv$$

$$= - k^2 \chi_i(k,\omega) \phi_{10} \ . \tag{17}$$

which yields the linear dielectric function $D(k,\omega)$ as

$$D(k,\omega) = 1 + \chi_e(k,\omega) + \chi_i(k,\omega) \ . \tag{18}$$

(The integral sub 0 means integration over zero order orbits.)

We now proceed to obtain the second order components. Assuming $\omega = \omega + i\delta$ and $\delta \to 0$, coefficients of d.c. terms of Eq. (14) give

$$f_{02} = \lim_{\delta \to 0} \frac{e}{M} \frac{ik}{2\delta} \left(-\phi_{10}^* \frac{\partial f_{10}}{\partial v} + \phi_{10} \frac{\partial f_{10}^*}{\partial v} \right) \ . \tag{19}$$

Substituting f_{10} by using Eq. (16), we get the quasilinear modification to the distribution function

$$f_{02} = \left| \frac{e\phi_{10}}{M} \right|^2 \frac{\partial}{\partial v} \left(\frac{\partial f_{oo}/\partial v}{(v-V)^2} \right) \ . \tag{20}$$

The component f_{11} results from the second order terms of Eq. (14) for $\exp(i\theta)$ as

$$f_{11} = \frac{e\phi_{11}}{M} \cdot \frac{\partial f_{oo}/\partial v}{v - V} \ . \tag{21}$$

Then, following a similar method used to derive Eq. (17) or Eq. (18), we obtain from Eq. (10)

$$D(k,\omega)\phi_{11} = 0 . \tag{22}$$

Coefficients of the second harmonic terms in Eq. (14) give

$$f_{02} = \frac{1}{2}\left(\frac{e\phi_{10}}{M}\right)^2 \frac{1}{v-V}\frac{\partial}{\partial v}\left(\frac{\partial f_{oo}/\partial v}{v-V}\right) + \frac{e\phi_{20}}{M}\frac{\partial f_{oo}/\partial v}{v-V} . \tag{23}$$

The first term appearing on the right side of Eq. (23) is the modification due to the bare second harmonic oscillation of a single wave, and the second term represents its shielding effect. Similarly, Eqs. (10) and (23) yield

$$\phi_{20} = \frac{\omega_{pi}^2}{8k^2 D(2k,2\omega)}\frac{e\phi_{10}^2}{M}\int_0 \frac{1}{v-V}\frac{\partial}{\partial v}\left(\frac{\partial f_{oo}/\partial v}{v-V}\right)dv . \tag{24}$$

For the third order component f_{12}, Eq. (14) gives

$$f_{12} = \frac{e}{M}\left(\phi_{10}\frac{\partial f_{02}/\partial v}{v-V} - \phi_{10}^{*}\frac{\partial f_{20}/\partial v}{v-V} + \phi_{12}\frac{\partial f_{oo}/\partial v}{v-V} + 2\phi_{20}\frac{\partial f_{10}^{*}/\partial v}{v-V}\right) . \tag{25}$$

Replacing f_{10}, f_{02} and f_{20} by Eqs. (16), (20) and (23), we get likewise

$$\begin{aligned} f_{12} = {} & \left|\frac{e\phi_{10}}{M}\right|^2 \cdot \left(\frac{e\phi_{10}}{M}\right)\left\{\frac{1}{v-V}\frac{\partial^2}{\partial v^2}\left(\frac{\partial f_{oo}/\partial v}{(v-V)^2}\right)\right. \\ & - \frac{1}{2}\frac{1}{v-V}\frac{\partial}{\partial v}\left(\frac{1}{v-V}\frac{\partial}{\partial v}\left(\frac{\partial f_{oo}/\partial v}{v-V}\right)\right) \\ & \left. + \frac{\omega_{pi}^2}{8k^2 D(2k,2\omega)}\left(\int_0 \frac{1}{v-V}\frac{\partial}{\partial v}\left(\frac{\partial f_{oo}/\partial v}{v-V}\right)dv\right)\cdot\frac{1}{v-V}\frac{\partial}{\partial v}\left(\frac{\partial f_{oo}/\partial v}{v-V}\right)\right\} . \end{aligned} \tag{26}$$

Substituting Eq. (26) into Eq. (10) for ϕ_{12} and using Eqs. (2), (17) and (22) yields the nonlinear dispersion relation

$$D(k,\omega)\tilde{\phi}_1 = \frac{\omega_{pi}^2}{k^2}\left\{\int_0 \frac{1}{v-V}\frac{\partial^2}{\partial v^2}\left(\frac{\partial f_{oo}/\partial v}{(v-V)^2}\right)dv\right.$$

$$-\frac{1}{2}\int_0 \frac{1}{v-V}\frac{\partial}{\partial v}\left(\frac{1}{v-V}\frac{\partial}{\partial v}\left(\frac{\partial f_{oo}/\partial v}{v-V}\right)\right)dv$$

$$\left.+\frac{\omega_{pi}^2}{8k^2D(2k,2\omega)}\left(\int_0 \frac{1}{v-V}\frac{\partial}{\partial v}\left(\frac{\partial f_{oo}/\partial v}{v-V}\right)dv\right)^2\right\}\cdot\left|\frac{e\tilde{\phi}_1}{M}\right|^2\cdot\tilde{\phi}_1$$

$$+\mathcal{O}(\varepsilon^4)\ . \qquad (27)$$

The first term on the right side is the nonlinear coupling of the potential with the quasilinear perturbation. The last two terms are the nonlinear coupling and shielding effect of the second harmonic potential with the fundamental perturbation. With the definition of

$$W(z) = v_{ti}^2\int_0 \frac{\partial f_{oo}/\partial v}{v-V}\,dv \qquad (28)$$

where $z = V/v_{ti} = \omega/kv_{ti}$, the quasilinear term gives

$$\int_0 \frac{1}{v-V}\frac{\partial^2}{\partial v^2}\left(\frac{\partial f_{oo}/\partial v}{(v-V)^2}\right)dv = \frac{1}{12v_{ti}^6}\frac{d^4W(z)}{dz^4}\ , \qquad (29)$$

the bare second harmonic effect becomes

$$-\frac{1}{2}\int_0 \frac{1}{v-V}\frac{\partial}{\partial v}\left(\frac{1}{v-V}\frac{\partial}{\partial v}\left(\frac{\partial f_{oo}/\partial v}{v-V}\right)\right)dv = -\frac{1}{16v_{ti}^6}\frac{d^4W(z)}{dz^4}\ , \qquad (30)$$

and the term associated with the shielded second harmonic oscillation is

$$\frac{\omega_{pi}^2}{8k^2 D(2k,2\omega)} \left[\int_0 \frac{1}{v - V} \frac{\partial}{\partial v} \left(\frac{\partial f_{oo}/\partial v}{v - V} \right) dv \right]^2$$

$$= \frac{1}{32k^2\lambda_D^2 \, v_{ti}^6 D(2k,2\omega)} \left(\frac{d^2 W(z)}{dz^2} \right)^2 . \qquad (31)$$

By using Eqs. (29), (30) and (31), we rewrite Eq. (27) as

$$D(k,\omega)\psi = \frac{1}{16k^2\lambda_D^2} \left[\frac{1}{3} \frac{d^4 W(z)}{dz^4} + \frac{1}{2k^2\lambda_D^2 D(2k,2\omega)} \left(\frac{d^2 W(z)}{dz^2} \right)^2 \right] |\psi|^2 \psi \qquad (32)$$

where $\psi = e\phi/T_i$ and λ_D is the ion Debye length. The quasilinear term and the bare second harmonic effect are combined in the first term of the right hand side in Eq. (32).

III. The Evolution Due to the Nonlinear Frequency Shift

In this section, we estimate the field energy at saturation caused by a finite nonlinear frequency shift by solving the nonlinear dispersion relation. As the wave amplitude is very small, Eq. (32) reduces to the usual linear dispersion

$$D(k,\omega) = D_R(k,\omega) + iD_I(k,\omega) . \qquad (33)$$

Let us examine Eq. (33) in the low drift velocity regime characterized by

$$|\gamma/\omega| \ll 1 \quad , \quad V \quad \text{and} \quad v_E \ll v_{ti} . \qquad (34)$$

The dielectric function for the Maxwellian ions is expressed as

$$D(k,\omega) = 1 + \frac{\omega_{pe}^2}{\omega_{ce}^2} + \frac{1}{k^2\lambda_D^2}\frac{\omega}{\omega - kv_E} + i\sqrt{\frac{\pi}{2}}\,\frac{1}{k^2\lambda_D^2}\frac{\omega}{|k|v_{ti}} \quad . \tag{35}$$

The real part of the frequency is determined to zeroth order in $|\gamma/\omega|$ by

$$D_R(k,\omega) = 1 + \frac{\omega_{pe}^2}{\omega_{ce}^2} + \frac{1}{k^2\lambda_D^2}\frac{\omega}{\omega - kv_E} = 0 \quad . \tag{36}$$

The solution is

$$\omega = \frac{k^2}{k^2 + k_m^2}\,kv_E \equiv \omega_o \tag{37}$$

and the growth rate $\gamma = -D_I/(\partial D_R/\partial\omega)_o$ is given by

$$\gamma = \sqrt{\frac{\pi}{2}}\,\frac{k^2/k_m^2}{(1 + k^2/k_m^2)^3}\,\frac{|k|}{k_m}\left(\frac{v_E}{v_{ti}}\right)^2\omega_{\ell h} \tag{38}$$

where

$$k_m = \left[\frac{1}{\lambda_D^2}\cdot\frac{1}{1 + \omega_{pe}^2/\omega_{ce}^2}\right]^{\frac{1}{2}} \tag{39}$$

is the wave number of the most unstable mode, and

$$\omega_{\ell h} = \frac{\omega_{pi}}{\sqrt{1 + \omega_{pe}^2/\omega_{ce}^2}} \tag{40}$$

is the lower hybrid frequency (Ref. 9). When the amplitude of the wave is

small but finite, expanding Eq. (32) around ω_o by replacing ω with $\omega_o + i(\partial/\partial t)$ and using Eqs. (35) and (36), we obtain

$$i\left[(1 + i\alpha)\frac{\partial}{\partial t} - \gamma\right]\psi = (A + iB)|\psi|^2\phi \tag{41}$$

where

$$\alpha \equiv (\partial D_I/\partial\omega)_o/(\partial D_R/\partial\omega)_o \doteq -\gamma/\omega_o \ , \tag{42}$$

$$A = -\frac{(\omega_o - kv_E)^2}{8kv_E}\left(\frac{4}{3} + \frac{1}{k^2\lambda_D^2 D_R(2k, 2\omega_o)}\right) \ , \tag{43}$$

and

$$B = -\frac{\gamma}{16}\left(5 + \frac{6}{k^2\lambda_D^2 D_R(2k, 2\omega_o)}\right) \ . \tag{44}$$

By using Eqs. (36) and (39), we get

$$\left[k^2\lambda_D^2 D_R(2k, 2\omega_o)\right]^{-1} = \frac{k_m^2}{k^2} \ . \tag{45}$$

Substituting Eq. (45) into Eqs. (43) and (44), and using Eqs. (29) through (32), the relative strengths of the nonlinear contributions from the quasi-linear modification, the bare second harmonic oscillation and its shielding are given as

$$A_{Q.L.} : A_{(2k,2\omega_o)_b} : A_{(2k,2\omega_o)_s} = 4 : -3 : \frac{k_m^2}{k^2} \tag{46}$$

and

$$B_{Q.L.} : B_{(2k,2\omega_o)_b} : B_{(2k,2\omega_o)_s} = 20 : -15 : 8\,\frac{k_m^2}{k^2} \ . \tag{47}$$

For the most unstable mode, $k = k_m$, the quasilinear modification on the ion distribution function is the dominant effect. For $\Psi = r \exp(is)$ where both r and s are real, Eq. (42) becomes

$$\alpha \dot{r} + r\dot{s} = - Ar^3 , \tag{48}$$

and

$$\dot{r} - \alpha r\dot{s} - \gamma r = Br^3 . \tag{49}$$

Eliminating r, we obtain

$$\dot{s} = - \frac{\alpha\gamma}{1+\alpha^2} - \frac{A+\alpha B}{1+\alpha^2} r^2 \tag{50}$$

where the first term is the linear correction to the frequency in the presence of growth, and the second term is the nonlinear frequency shift which grows in time with r^2 (i.e., $|e\phi/T_i|^2$).

Eliminating $r\dot{s}$, we obtain

$$\dot{r} = \left(\frac{\gamma}{1+\alpha^2} + \frac{B - \alpha A}{1+\alpha^2} r^2 \right) r . \tag{51}$$

Integration of Eq. (51) yields

$$r^2 = r_\infty^2 \frac{ce^{2\gamma t/(1+\alpha^2)}}{1 + ce^{2\gamma t/(1+\alpha^2)}} \tag{52}$$

where

$$r_\infty^2 \equiv \left| \frac{e\phi}{T_i} \right| (t \to \infty) = \sqrt{\frac{\gamma}{\alpha A - B}} \tag{53}$$

is the field energy level at saturation. From Eqs. (42) through (47),) it is obvious that the quasilinear effect and the shielded second harmonic oscillation stabilize a single lower-hybrid drift wave, i.e., that they lower the saturation level. The nonlinearity due to the bare second harmonic oscillation of the wave raises the saturation level. If $r_\infty \gg r(t=0) = r_o$, Eq. (52) gives

$$r^2(t) = \frac{r_o^2 \, e^{\frac{2\gamma t}{1+\alpha^2}}}{1 + \frac{r_o^2}{r_\infty^2} e^{\frac{2\gamma t}{1+\alpha^2}}} \tag{54}$$

and Eq. (50) becomes

$$\dot{s}(t) = -\frac{\alpha\gamma}{1+\alpha^2} - \frac{A+\alpha B}{1+\alpha^2} \frac{r_o^2 \, e^{\frac{2\gamma t}{1+\alpha^2}}}{1 + \frac{r_o^2}{r_\infty^2} e^{\frac{2\gamma t}{1+\alpha^2}}} \, . \tag{55}$$

IV. Conclusion

The nonlinear dispersion relation was derived. We obtained the saturation field energy and the nonlinear frequency shift at saturation caused by the frequency shift only. With use of Eqs. (35) through (44), Eq. (53) gives

$$\left| \frac{e\phi}{T_i} \right|^2_{sat} = \left(\frac{5}{16} + \frac{k_m^2}{2k^2} + \frac{k_m^4}{6k^4} \right)^{-1} . \tag{56}$$

Therefore, the nonlinear frequency shift will stabilize the lower-hybrid drift instability at small amplitudes only if $k \ll k_m$. For the most unstable mode, $k = k_m$, we expect that other nonlinear effects will be the dominant saturation mechanism such as trapping, quasilinear diffusion, etc.

REFERENCES

1. R. C. Davdison, N. T. Gladd, C. S. Wu, and J. D. Huba, "Effects of Finite Plasma Beta on the Lower-Hybrid Drift Instability", Phys. Fl. 20, 301 (1977).
2. Y. H. Ichikawa, T. Imamura and T. Taniuti, "Nonlinear Wave Modulation in Cotlisionless Plasma", J. Phys. Soc. Japan 33, 189 (1972).
3. H. Sanuki, K. Shimizu and J. Todoroki, "Effects of Landau Damping on Nonlinear Wave Modulation in Plasma", J. Phys. Soc. Japan 33, 198 (1972).
4. A. K. Nekrason, "Non-Linear Evolution of Drift-Cyclotron Flute Oscillations", Nuclear Fusion 14, 865 (1974).
5. R. E. Aamodt, Y. C. Lee, C. S. Liu and M. N. Rosenbluth, "Nonlinear Dynamics of Drift-Cyclotron Instability", Phys. Rev. Lett. 39, 1660 (1977).
6. R. E. Aamodt, Y. C. Lee, C. S. Liu, D. R. Nicholson, M. N. Rosenbluth and B. I. Cohen, to be published.
7. R. C. Myer and A. Simon, to be published; and R. C. Myer, Ph.D. thesis, Univ. of Rochester (1979).
8. B. I. Cohen and N. Maron, "Simulation of Drift-Cone Modes", LLL report UCRL-83260 (1979), to be published.
9. R. C. Davidson, "Quasi-Linear Stabilization of Lower-Hybrid-Drift

Instability", Phys. Fl. 21, 1375 (1978).

10. J. D. Huba and K. Papadopoulos, "Nonlinear Stabilization of the Lower-Hybrid-Drift Instability by Electron Resonance Broadening", Phys. Fl. 21, 121 (1978).

E. CONTROL OF UNWANTED BEAMING INSTABILITIES

Yu Jiuan Chen (Prof. C. K. Birdsall)

No new work this quarter.

It is planned to look into similar instabilities which occur in magnetized plasmas with a Maxwellian or other $f(\underline{v}_\perp)$ made up of rings in $v_\perp$ space at $t = 0$. The multi-ring dispersion relation will be solved for complex ω and real k. Instabilities are expected even with a Maxwellian distribution. Simulations will be done to find saturation levels and detailed ring-ring interaction in order to aid in finding means of control of these physical but unwanted instabilities.

F. TRANSVERSE OSCILLATIONS OF A CURRENT SHEET IN A PLASMA - THEORY

Alex Friedman

We consider the problem of an infinitesimally thin current sheet of ions, in a background plasma bounded by conducting walls. The configuration is illustrated in Fig. 1; the sheet current J^0 flows in the $+\hat{y}$ direction, the zero order magnetic field is in the $+\hat{z}$ direction for $x < 0$ and in the $-\hat{z}$ direction for $x > 0$, and the system

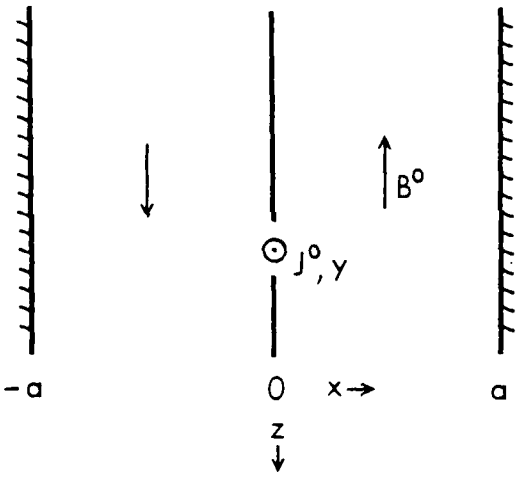

Figure 1. Configuration of current sheet in plasma.

is bounded by metallic walls at $x = \pm a$. We consider rigid displacements of the sheet in the $\hat{x}$ direction given by $\varepsilon \exp(-i\omega t)$.

The zero order magnetic field is given by:

$$-\frac{\partial B^0}{\partial x} = J_y^0 = qv_0\delta(x), \tag{1}$$

where the zero order current is entirely in the $\hat{y}$ direction:

$$\underline{J}^0 = qv_0\delta(x)\hat{y} \tag{2}$$

The first order current due to the sheet is then given by:

$$\underline{J}^1_s = q\varepsilon[-v_0\frac{\partial}{\partial x}\delta(x)\hat{y} - i\omega\delta(x)\hat{x}\ ]\ e^{-i\omega t}. \tag{3}$$

(there is no v^1_y term arising from $\underline{\xi} \times \underline{B}^0$ because B^0 is zero at the sheet).

The equation of motion of the sheet is:

$$-\omega^2\varepsilon = v_0\Omega^1_{plasma}, \tag{4}$$

where Ω is the cyclotron frequency qB/mc, and q/m is the sheet's charge/mass ratio; since the sheet cannot exert a force upon itself, Ω^1_{sheet} is cancelled by $(\varepsilon\partial/\partial x)\Omega^0$.

The analysis proceeds in a manner analogous to that of Ref. 1. The plasma response is given by:

$$\rho\dot{\underline{v}}^1 = \underline{j}^1_\rho \times \underline{B}^0/c, \tag{5}$$

$$\underline{E}^1 + \underline{v}^1_e \times \underline{B}^0/c = 0, \tag{6}$$

which implies, since B^0 is zero at the sheet, that E^1 is zero at the sheet, and thus the equation of motion above does not involve E^1, and any excess electrons accompanying the sheet (to provide charge neutrality) provide no current. The field equations are:

$$c\nabla \times \underline{B}^1 = 4\pi(\underline{j}_\rho + \underline{j}_s), \tag{7}$$

$$c\nabla \times \underline{E}^1 = i\omega \underline{B}^1. \tag{8}$$

Combining eqns. (6) and (8), taking the cross product of eqn. (5) with $\underline{B}^0$, and combining the resulting equations, yields:

$$\begin{aligned} -\omega^2 \underline{B}^1 = v_A^2 \left[\frac{4\pi}{c} \nabla \times j_{s\perp} - \nabla \times (\nabla \times \underline{B}^1)_\perp \right] \\ + \nabla v_A^2 \times \left[\frac{4\pi}{c} j_s - \nabla \times \underline{B}^1 \right]_\perp \\ + i\omega \nabla \times [(\underline{j}/nec) \times \underline{B}^0], \end{aligned} \tag{9}$$

The Alfven speed v_A is defined as $B^0/(4\pi\rho)^{1/2}$, and we have used the relation $v_e = v - j/ne$. The last term on the right of equation (9) is zero, since it is equal to $(i\omega/nec)\partial/\partial x(-j_x B^0)$, and j_x is zero because $\hat{x} \cdot (\nabla \times \underline{B}^1)$ is zero.

Using Eqn. (3) for j_s, and taking the $\hat{z}$ component, yields

$$\begin{aligned} [\partial^2/\partial x^2 + \omega^2/v_A^2 + (2/v_A)(\partial v_A/\partial x)\partial/\partial x] B^1 \\ = (4\pi/c) q\varepsilon v_0 [\partial^2/\partial x^2 + (2/v_A)(\partial v_A/\partial x)\partial/\partial x]\delta(x), \end{aligned} \tag{10}$$

where the subscript z of B_z^1 has been omitted. We define a quantity b equal to the first order magnetic field everywhere but at the sheet itself by:

$$b = B^1 - (4\pi/c) q\varepsilon v_0 \delta(x), \tag{11}$$

so that

$$[\partial^2/\partial x^2 + \omega^2/v_A^2 + (2/v_A)(\partial v_A/\partial x)\partial/\partial x] b = -(4\pi/c) q\varepsilon v_0 (\omega^2/v_A^2)\delta(x). \tag{12}$$

Using the relation $(2/v_A)(\partial v_A/\partial x)(\partial b/\partial x) = (1/v_A^2)\partial/\partial x(v_A^2 \partial b/\partial x) -$

$\partial^2 b/\partial x^2$, this simplifies to:

$$b + \partial/\partial x[(v_A^2/\omega^2)\partial b/\partial x] = -(4\pi/c)q\varepsilon v_0\delta(x). \tag{13}$$

By integrating this equation across the layer two jump conditions are obtained:

$$\left[\frac{v_A^2}{\omega^2}\frac{\partial b}{\partial x}\right] = -\frac{4\pi}{c}q\varepsilon v_0, \tag{14}$$

$$[\,b\,] = 0. \tag{15}$$

We specify a boundary condition corresponding to zero plasma density at the wall,

$$\left.\frac{\partial B^1}{\partial x}\right|_{x=\pm a} = 0 \tag{16}$$

A particular solution of Eqn. (13) is

$$b_{part} = -(2\pi/c)q\varepsilon v_0(\omega/v_A)\sin(\omega|x|/v_A). \tag{17}$$

This solution satisfies the jump conditions at the layer but not the boundary conditions at the two walls, so we add in a constant α times the homogeneous solution $\cos(\omega x/v_A)$, which is symmetric about $x = 0$. Then, using the boundary conditions (16),

$$\partial b/\partial x = \mp(2\pi/c)q\varepsilon v_0(\omega^2/v_A^2)\cos(\omega x/v_A) - \alpha(\omega/v_A)\sin(\omega x/v_A), \tag{18}$$

where

$$\alpha = -(2\pi/c)q\varepsilon v_0(\omega/v_A)\cot(\omega a/v_A). \tag{19}$$

Keeping only the plasma contribution to Ω^1, as noted after Eqn. (4), we use b and not B^1 to find the appropriate value of $\Omega^1(x=0)$:

$$-\omega^2\varepsilon = v_0\Omega^1_{plasma} = -(2\pi/c^2)(qe\varepsilon v_0^2/m)(\omega/v_A)\cot(\omega a/v_A). \tag{20}$$

or, more concisely,

$$X \tan X = Y, \tag{21}$$

where

$$X = \omega a/v_A, \text{ and } Y = 2\pi qe v_0^2 a/mc^2 v_A^2 > 0. \tag{22}$$

Note that Y is real and positive. This equation has an infinite number of discrete, stable solutions for X, which can be obtained in a graphical manner by rewriting Eqn. (21) in the form:

$$\cot X = X/Y \tag{23}$$

and plotting both sides as functions of X on the same axes (see Fig. 2); it is easy to prove that no unstable solutions exist. Furthermore, for large values of Y the roots fall near $X = \pm\pi/2, \pm 3\pi/2, \ldots$, while for small Y the roots fall near $X = 0$ (double root), $\pm\pi, \pm 2\pi, \ldots$

It is not difficult to extend the calculation to cases where the layer is not equidistant from two walls at $x = -a_1$ and $x = a_2$. Such an equilibrium requires the existance of a uniform externally supplied magnetic field (in this sense it more closely resembles the cylindrically-symmetric current layer than does the centered-sheet

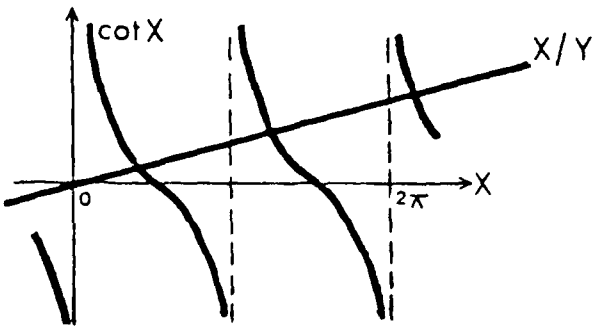

Figure 2. Graphical solution for root of centered-sheet problem.

case); alternately, it may be considered as arising from the introduction of the conducting walls after the layer is in place, thus freezing the equilibrium flux appropriately. The particular solution (17) is unchanged, but now the antisymmetric homogeneous solution must be included; we thus add in $\alpha \cos(\omega x/v_A) + \beta \sin(\omega x/v_A)$, and find

$$\alpha = \frac{-(4\pi/c)qev_0\omega/v_A}{\tan(\omega a_1/v_A) + \tan(\omega a_2/v_A)} \tag{24}$$

where for the normal mode frequencies (but not for the mode structure) the value of β is irrelevant since the field at the layer is the only value of importance. Defining

$$K = a_2/a_1,\ X = \omega a_1/v_A,\ \text{and}\ Y = 2\pi qev_0^2 a_1/mc^2 v_A^2 \tag{25}$$

we find the normal mode frequencies to be given by

$$X\,[\,\tan X + \tan KX\,]\,/\,2 \;=\; Y, \tag{26}$$

where Y and K are real and positive, and with no loss of generality we

can choose $0 < K \leq 1$. A graphical solution (for $K = 0.8$) appears in

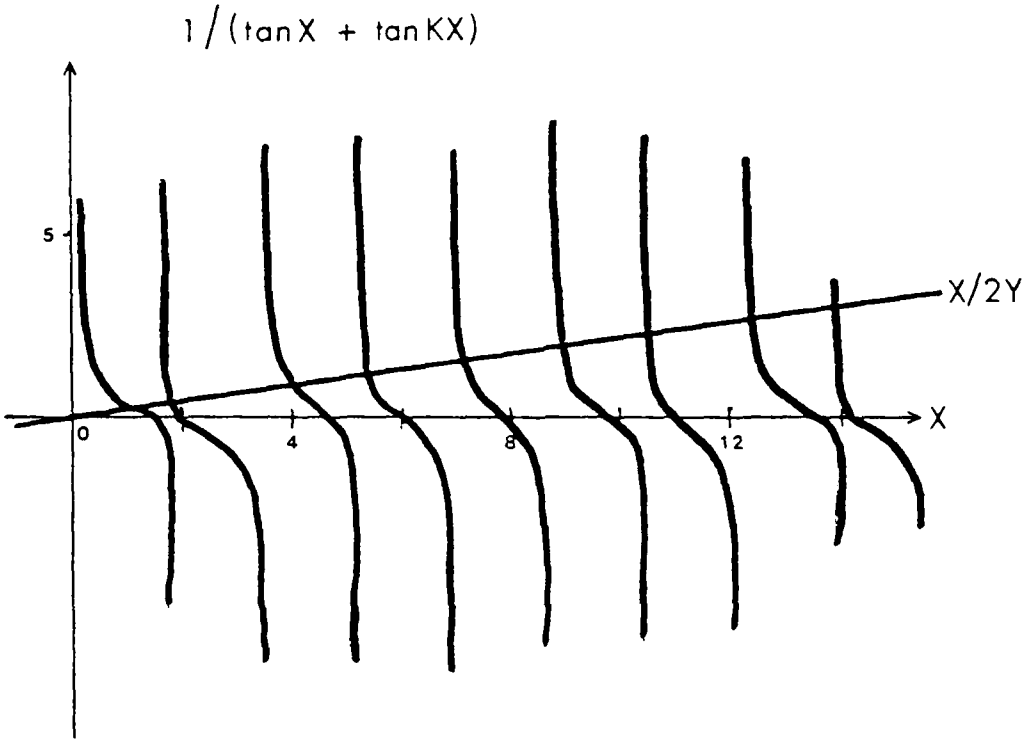

Figure 3. Graphical solution of uncentered-sheet problem for $K = 0.8$.

Fig. 3. Due to cancellations of the two different tangent terms, twice as many roots are present as in the centered-sheet case. For small Y new roots at $\pm\pi/2$, $\pm 3\pi/2$, etc. join those at $\pm\pi$, $\pm 2\pi$, ... For large Y each root splits into two, but these remain close together and near $\pm\pi/2$, $\pm 3\pi/2$ etc. when $K \approx 1$. For large Y (dense plasma), i.e. when α is near zero, the wave is localized to one side of the sheet or the other depending upon which of the "split" solutions for X is chosen. The wave is "resonant" with either the left cavity or the right, and so is of large amplitude (has a large B^1) only in that

cavity, while in the other cavity the wave suffers destructive interference between the particular and homogeneous parts of the solution. When γ is small, α is large and the mode is not localized, as expected.

The author wishes to acknowledge useful discussion with M. Carver, and with D. Harned, whose simulations of this system are presented elsewhere in this Report.

---

[1] H.L. Berk and R.N. Sudan, "E-layer Precession in a Plasma," J. Plasma Phys. 6, 413 (1971).

G. TRANSVERSE OSCILLATIONS OF A CURRENT SHEET IN A PLASMA — SIMULATION

Doug Harned (Alex Friedman, Prof. C. K. Birdsall)

Our one-dimensional quasineutral hybrid code QUAD1 (previous QPR) was used to study the oscillations of a thin sheet of ions propagating through a cold background plasma. Conducting wall boundary conditions were used. The geometry of this configuration is shown in Fig. 1 of the previous section. This problem is analogous to the cylindrical problem of the m = 0 oscillation of a field-reversing ion-layer in the limit of infinite radius.

Simulations were performed by placing a beam of one cell-width in a uniform plasma and then applying a small rigid perturbation in the x-direction. Our simulations have demonstrated the stability of such a system. The measured layer oscillation frequencies were found to agree well with analytic results derived in the preceding section. We will define x_w as the half-width of the plasma slab, v_A as the Alfven velocity, v_o as the beam velocity, and M_b as the total mass of the beam. The charge-to-mass ratios for the beam and the background plasma have been assumed to be identical. The analytic expression for the oscillation frequency of the beam,

$$X \tan X = Y \tag{1}$$

where

$$X \equiv \frac{\omega x_w}{V_A} \tag{2}$$

$$Y \equiv \frac{2\pi e^2 v_o^2 x_w M_b}{m^2 c^2 V_A^2} \tag{3}$$

was solved for the lowest harmonic with a root-solver (SOLVER[2]) and is plotted in Fig. 1. The values obtained from our simulations are indicated on the graph.

The parameter Y on the right side of Eq. 1 may be expressed as the ratio of the total background plasma mass to the mass of the beam:

$$Y = \frac{2x_w m n_p}{M_b} = \frac{M_p}{M_b} \tag{4}$$

There are two limiting cases.

When $M_p/M_b \gg 1$ the inertia of the beam is not important. An initial perturbation to the right sends a compressional Alfven wave to the right wall. After the wave has reflected and returned to the center, the beam feels a force to the left. This motion sends a new compressional Alfven wave toward the left wall. The beam continues to oscillate about the center in this manner, with a period equal to the time required for an Alfven wave to traverse the slab twice, i.e.,

$$\omega = \frac{\pi v_A}{x_w} \tag{5}$$

An example of this type of motion is shown in Fig. 2.

If the mass of the beam is increased (or the background density decreased) the inertia of the beam slows its response to the wave, reducing the frequency. For the case $M_p/M_b \ll 1$ the plasma response is negligible and the motion of the beam is that of a simple harmonic oscillator, with the only force being due to the magnetic pressure gradient across the beam. The equation of motion is

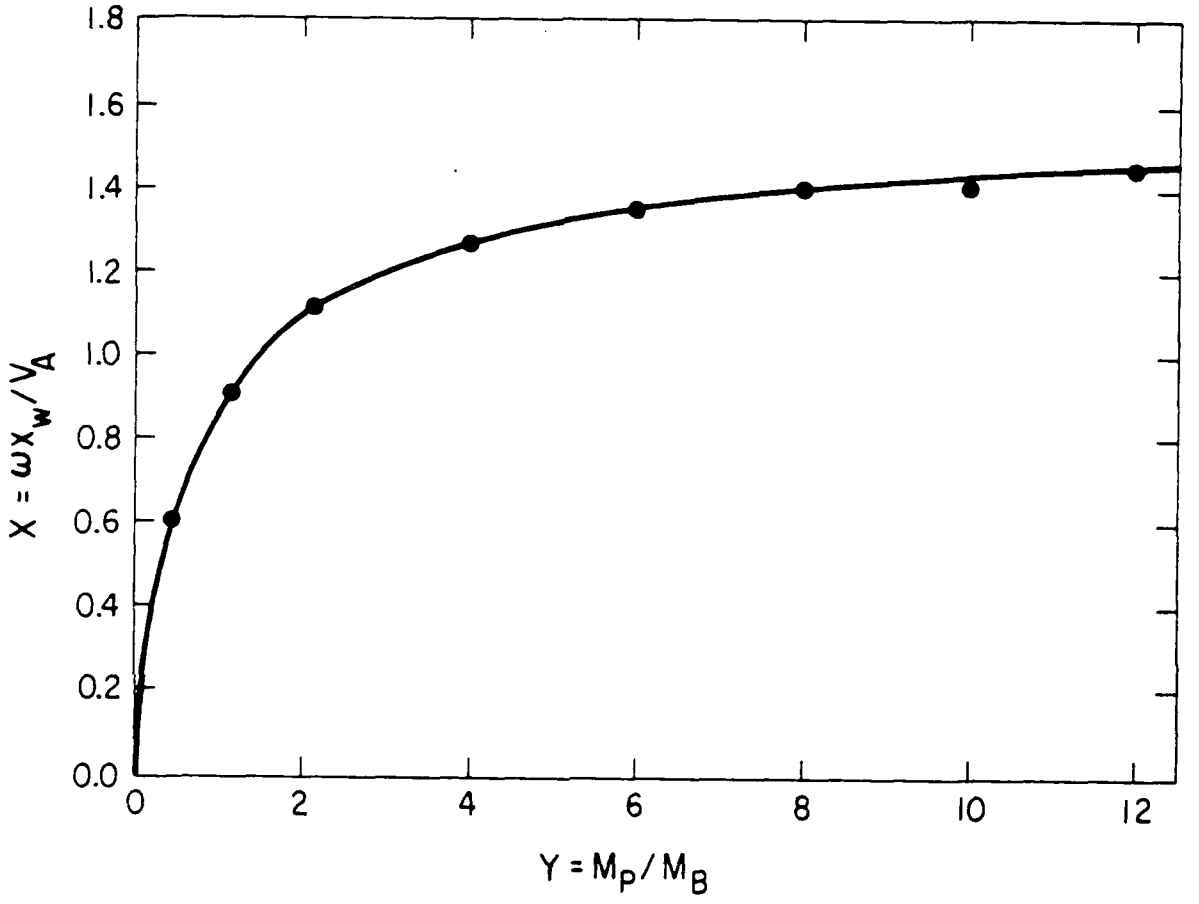

FIG. 1 Results of theory and simulation. The solution for the lowest harmonic from Eq. 1 is plotted. The circles represent the simulation results.

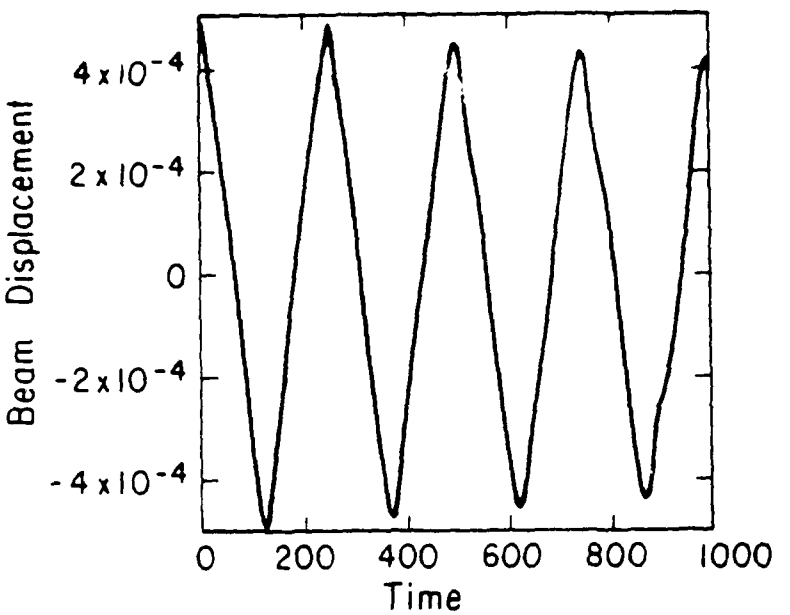

FIG. 2 Motion of perturbed beam showing triangular oscillations for $M_p/M_b = 60$.

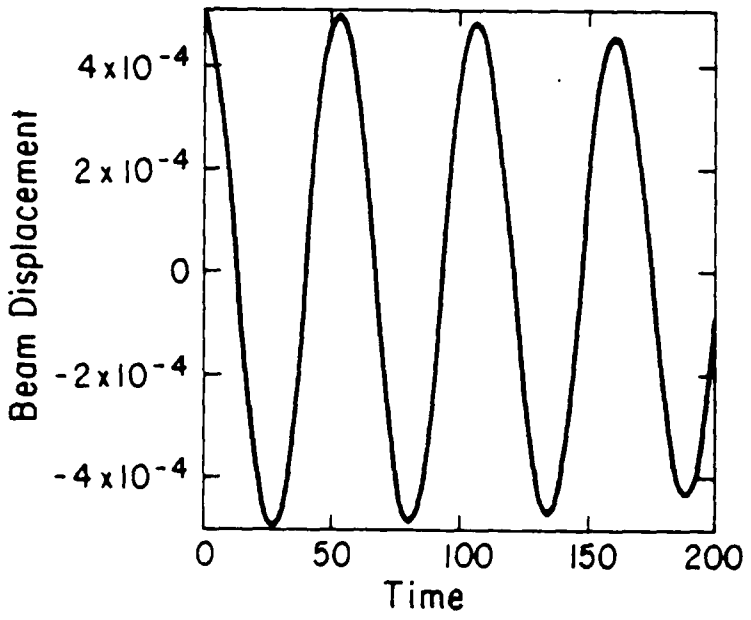

FIG. 3 Motion of perturbed beams showing sinusoidal oscillations for $M_p/M_b = .6$.

$$m \frac{\partial^2 \xi}{\partial t^2} = -\nabla \left(\frac{B^2}{8\pi} \right). \tag{6}$$

Integration across the layer gives

$$- M_b \frac{\partial^2 \xi}{\partial t^2} = \frac{B_o^2}{8\pi} x_w \left(\frac{1}{(x_w - \xi)^2} - \frac{1}{(x_w + \xi)^2} \right) \tag{7}$$

where B_o is the equilibrium magnetic field. Writing $\xi = \xi e^{i\omega t}$ and performing a Taylor expansion on the right side of Eq. 7, the oscillation frequency is found to be

$$\omega = B_o \sqrt{\frac{1}{2\pi M_b x_w}} \tag{8}$$

An example of this type of behavior is shown in Fig. 3. It should be noted that the beam moves with sinusoidal oscillations, rather than with the triangular oscillations which occur when the effect is due solely to Alfven wave reflections (Fig. 2). Eqs. 5 and 8 represent the high and low frequency limits, respectively, of the lowest harmonic of Eq. 1 (Fig. 1).

H. FIELD REVERSED PLASMA SIMULATIONS, QUASINEUTRAL, in 2d

Doug Harned (Dr. Alex Friedman Prof. C. K. Birdsall)

We are currently testing a two-dimensional quasineutral code, AQUARIUS (A QUasineutral AlgoRithm for Ion Simulation). The purpose of this code is to study the behavior of systems characterized by large ion gyroradii and long time scales ($t > \Omega_i^{-1}$, where Ω_i is the ion-cyclotron frequency). Examples of such systems are field-reversed mirrors and ion layers. Although these particular systems have cyclindrical shape, cartesian coordinates were chosen for AQUARIUS. While cartesian coordinates make the application of cylindrical diagnostics and boundary conditions more difficult, they avoid the problems of poor resolution at large radii and the singularity of the origin at small radii, often associated with cylindrical coordinates. In our r-θ code, there is added limitation that a Courant condition ($\Delta t < \frac{\Delta x}{v_A}$) must be satisfied throughout the system. This limitation governs the fineness of the grid near the origin which in turn may force one to pay a substantial penalty either in accuracy at large radii or in computational time (if small time step is used to allow a reduction in Δx). Cartesian coordinates will allow the treatment of a wide variety of plasma configurations, including infinite systems, for which cylindrical coordinates are not well suited (e.g., periodic boundaries cannot be applied in the radial direction). Cartesian coordinates have added advantages in that equations in the field-solver are simpler and avoid difficulties that can arise in cylindrical particle movers.

AQUARIUS is similar to our one-dimensional code, QUAD1 (see last QPR). It is non-linear, uses PIC techniques to advance the particles

and employs a quasineutral Darwin field solver. As in QUAD1, the electric field is advanced with the Darwin approximation of Ampere's law

$$\nabla \times \underline{B} = \frac{4\pi \underline{J}}{c} \tag{1}$$

and the inertialess electron momentum equation, which for cold electrons can be written as

$$\underline{E} + \frac{\underline{v}_e}{c} \times \underline{B} = 0 . \tag{2}$$

Combining Eqs. 1 and 2, we have

$$\underline{E} = \frac{1}{4\pi ne} (\nabla \times \underline{B}) \times \underline{B} - \frac{1}{nec} \underline{J}_i \times \underline{B} . \tag{3}$$

In two dimensions this expression reduces to

$$\underline{E} = \frac{1}{4\pi ne} \nabla B_z^2 - \frac{1}{nec} \underline{J}_i \times B_z \hat{z} . \tag{4}$$

The magnetic field is advanced with Faraday's law,

$$\frac{\partial B_z}{\partial t} \hat{z} = -c \nabla \times \underline{E} \tag{5}$$

which completes the field solver. Eqs. 4 and 5 are solved as in QUAD1, using a predictor-corrector method like that of Byers et al.[1] One predictor-corrector iteration was found to be sufficient for the fields to converge.

Because the successive application of Eqs. 4 and 5 constitutes two spatial derivatives of the electric field, some care was required to avoid the appearance of an alternating-cell instability. Such an instability will occur if $\underline{E}$ and $\underline{B}$ are determined using simple centered differences to represent spatial derivatives on a single grid. To avoid this problem we are using interlaced grids for the electric and magnetic fields. Centered differences can then be applied effectively.

The code has been tested on cold Alfven waves. The waves were found to have correct frequencies and propagation speeds along the horizontal and vertical directions, as well as at an angle of 45°. Some error has been observed at intermediate angles due to the squareness of the present difference operators in the code. We are presently using four-point operators to represent derivatives for both the curl and gradient operations. Such operators exhibit angle errors[2] proportional to $(k\Delta x)^2$, which become severe at large values of $k\Delta x$. We would like to reduce the angle errors presently seen in AQUARIUS. While some improvement has been obtained by smoothing, it may be possible to further reduce the angle error by the implementation of a higher order operator.

Twelve-point operators can be derived for the gradient and the curl. Figure 1 shows the grid points used in the four and twelve-point operators. Derivatives in each direction may be written as

$$\left(\frac{\partial U}{\partial x}\right)_{i,j} = \frac{1}{4h(1+\alpha+3\beta)}\Big[U_{i+1,j+1}+U_{i+1,j-1}-U_{i-1,j+1}-U_{i-1,j-1}$$

$$+\alpha\left(U_{i+1,j+3}+U_{i+1,j-3}-U_{i-1,j+3}-U_{i-1,j-3}\right)$$

$$+\beta\left(U_{i+3,j+1}+U_{i+3,j-1}-U_{i-3,j+1}-U_{i-3,j-1}\right)\Big]$$

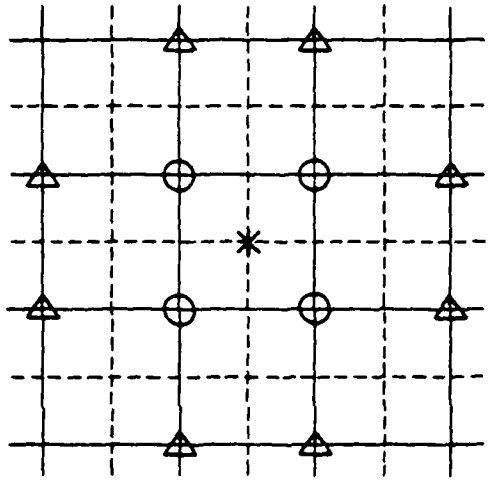

FIG. 1 Twelve-point and four-point operators. The dashed lines represent the grid for $\underline{V}$ and the solid lines represent the grid for U. To obtain $\underline{V}$ at the point x, from the equation $V = -\Delta U$, one may use (a) a four-point operator, using the points denoted by circles, or (b) a twelve-point operator which uses, in addition to those of the four-point operator, the points denoted by triangles.

$$- \frac{h^2}{2(1+\alpha+3\beta)} \left\{ \frac{1}{3} (1+\alpha+27\beta) \frac{\partial^3 U}{\partial x^3} + (1+9\alpha+3\beta) \frac{\partial^3 U}{\partial x \partial y^2} + \ldots . \right\}$$

where h is the grid spacing ($h = \Delta x = \Delta y$). α and β are adjustable parameters. If α and β are both set to zero, the second-order accurate four-point operator is obtained:

$$\frac{\partial U}{\partial x} = \frac{1}{4h} \left(U_{i+1,j+1} + U_{i+1,j-1} - U_{i-1,j+1} - U_{i-1,j-1} \right)$$

$$- \frac{h^2}{6} \left(\frac{\partial^3 U}{\partial x^3} + 3 \frac{\partial^3 U}{\partial x \partial y^2} \right) + \ldots \quad . \tag{6}$$

By appropriately adjusting α and β, it is possible to obtain fourth-order accuracy in the twelve-point operator. However, it would be more desirable to minimize the angle error in order to reduce the effects of the grid squareness on cylindrical problems.

Consider the gradient operator, $\underline{V} = -\nabla u$, where u is a scalar potential. Using the twelve-point operator, and writing u as $u = u_o e^{ik_x x} \cdot e^{ik_y y}$, the gradient can be expressed by

$$V_x = \frac{-1}{(4+4\alpha+12\beta)} \left[\left(\frac{e^{i\frac{1}{2}k_x\Delta x} - e^{-i\frac{1}{2}k_x\Delta x}}{\Delta x} \right) \left(e^{i\frac{1}{2}k_y\Delta y} + e^{-i\frac{1}{2}k_y\Delta y} \right) \right.$$

$$+ \alpha \left(\frac{e^{i\frac{1}{2}k_x\Delta x} - e^{-i\frac{1}{2}k_x\Delta x}}{\Delta x} \right) \left(e^{i\frac{3}{2}k_y\Delta y} + e^{-i\frac{3}{2}k_y\Delta y} \right)$$

$$\left. + \beta \left(\frac{e^{i\frac{3}{2}k_x\Delta x} - e^{-i\frac{3}{2}k_x\Delta x}}{\Delta x} \right) \left(e^{i\frac{1}{2}k_y\Delta y} + e^{-i\frac{1}{2}k_y\Delta y} \right) \right] u \tag{7a}$$

$$V_y = \frac{1}{(4+4\alpha+12\beta)} \left[\left(\frac{e^{i\frac{1}{2}k_y\Delta y} - e^{-i\frac{1}{2}k_y\Delta y}}{\Delta y} \right) \left(e^{i\frac{1}{2}k_x\Delta x} + e^{-i\frac{1}{2}k_x\Delta x} \right) \right.$$

$$+ \alpha \left(\frac{e^{i\frac{1}{2}k_y\Delta y} - e^{-i\frac{1}{2}k_y\Delta y}}{y} \right) \left(e^{i\frac{3}{2}k_x\Delta x} + e^{-i\frac{3}{2}k_x\Delta x} \right)$$

$$\left. + \beta \left(\frac{e^{i\frac{3}{2}k_y\Delta y} - e^{-i\frac{3}{2}k_y\Delta y}}{\Delta y} \right) \left(e^{i\frac{1}{2}k_x\Delta x} + e^{-i\frac{1}{2}k_x\Delta x} \right) \right] u \, . \qquad (7b)$$

Defining $X=k_x\Delta x$, $Y=k_y\Delta y$, and $dif(x) = \frac{\sin x}{x}$, Eqs. 7 reduce to

$$V_x = \frac{i}{(1+\alpha+3\beta)} \left[\frac{k_x}{2} dif \frac{X}{2} \cos \frac{Y}{2} + \alpha \frac{k_x}{2} dif \frac{X}{2} \cos \frac{3Y}{2} \right.$$

$$\left. + 3\beta \frac{k_x}{2} dif \frac{3X}{2} \cos \frac{Y}{2} \right] u \qquad (8a)$$

$$V_y = \frac{i}{(1+\alpha+3\beta)} \left[\frac{k_y}{2} dif \frac{Y}{2} \cos \frac{X}{2} + \alpha \frac{k_y}{2} dif \frac{Y}{2} \cos \frac{3X}{2} \right.$$

$$\left. 3\beta \frac{k_y}{2} dif \frac{3Y}{2} \cos \frac{X}{2} \right] u \, . \qquad (8b)$$

Since $\underline{V} = i\underline{k}u$, we have*

$$\frac{K_{x_{12}}}{k_x} = \frac{\frac{1}{2}}{(1+\alpha+3\beta)} \left[dif \frac{X}{2} \cos \frac{Y}{2} + \alpha dif \frac{X}{2} \cos \frac{3Y}{2} + 3\beta dif \frac{3X}{2} \cos \frac{Y}{2} \right] \qquad (9a)$$

$$\frac{K_{y_{12}}}{k_y} = \frac{\frac{1}{2}}{(1+\alpha+3\beta)} \left[dif \frac{Y}{2} \cos \frac{X}{2} + \alpha dif \frac{Y}{2} \cos \frac{3X}{2} + 3\beta dif \frac{3Y}{2} \cos \frac{X}{2} \right], \qquad (9b)$$

where $\underline{K}_{12}$ is the effective wave vector produced by the twelve-point operator. It is possible to compute the angle error (A_{12}) of the twelve-point operator. The angle error is defined as the sine of the angle between the actual wave vector, $\underline{k}$, and the finite difference approximation, $\underline{K}_{12}$, following Ref. 2,

$$A_{12} \equiv \sin\theta_{12} = \frac{|\underline{k} \times \underline{K}_{12}|}{|\underline{k}||\underline{K}_{12}|} = \frac{XY\left|\frac{K_y}{k_y} - \frac{K_x}{k_x}\right|}{\sqrt{X^2+Y^2}\sqrt{\frac{K_x^2}{k_x^2}X^2 + \frac{K_y^2}{k_y^2}Y^2}} \quad . \quad (10)$$

The angle error will be minimized when the numerator,

$$XY\left|\frac{1}{(X/2)}\left(\sin\frac{X}{2}\cos\frac{Y}{2} + \alpha\sin\frac{X}{2}\cos\frac{3Y}{2} + \beta\sin\frac{3X}{2}\cos\frac{Y}{2}\right)\right.$$

$$\left. - \frac{1}{(Y/2)}\left(\sin\frac{X}{2}\cos\frac{X}{2} + \alpha\sin\frac{Y}{2}\cos\frac{3X}{2} + \beta\sin\frac{3Y}{2}\cos\frac{X}{2}\right)\right| \quad (11)$$

goes to zero. A Taylor expansion may be performed on the sines and cosines:

$$\frac{1}{(X/2)}\sin\frac{X}{2} = 1 - \frac{\left(\frac{X}{2}\right)^2}{3!} + \frac{\left(\frac{X}{2}\right)^4}{5!} + \ldots . \quad (12a)$$

$$\cos\frac{X}{2} = 1 - \frac{\left(\frac{X}{2}\right)^2}{2!} + \frac{\left(\frac{X}{2}\right)^4}{4!} + \ldots . \quad . \quad (12b)$$

When these expansions are used in Eq. 11, and terms beyond second order are dropped, the following expression is obtained to minimize the error:

$$1 - 9\alpha + 3\beta = 0 . \qquad (13)$$

This equation provides a means of determining α and β to give accuracy in angle to $(k\Delta x)^4$ for small $k\Delta x$. The freedom to choose one parameter is still available and this may be done to effect some reduction in magnitude error. If the derivatives in the second-order, magnitude error terms ($\partial^3 u/\partial x^3$ and $\partial^3 u/\partial x \partial y^2$) are assumed to be comparable, then the optimum values of α and β are found to be -.04 and .0533, respectively. Figure 2 provides a comparison between the angle errors (from Eqs. 9 and 10) given by this twelve-point operator and the standard four-point operator. In Fig. 2 the minimum angle errors, which occur at an angle $\pi/8$ relative to either the x or y axis, are plotted for each operator ($\alpha = -.04$, $\beta = .0533$ for the twelve-point operator).

REFERENCES

1. J. A. Byers, B. I. Cohen, W. C. Condit, J. D. Hanson, "Hybrid Simulations of Quasineutral Phenomena in Magnetized Plasmas", J. Computational Phys. 27, 367-396 (1968).

2. C. K. Birdsall, A. B. Langdon, Plasma Physics Via Computer Simulation (1978), Chapter 14.

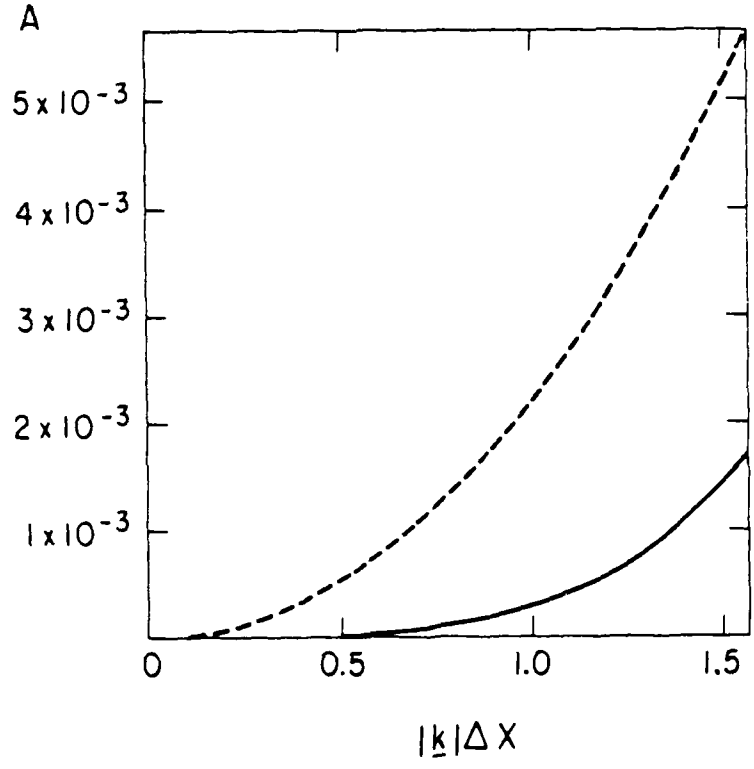

FIG. 2 Maximum angle error, A, versus $|\underline{k}|\Delta x$. The dotted line is for the four-point operator. The solid line is for the twelve-point operator and shows substantial improvement at small $|\underline{k}|\Delta x$.

I. FIELD REVERSED PLASMA STABILITY;
LINEARIZED SIMULATIONS IN 3D*

Alex Friedman

(The following is an abstract submitted as a contribution to "The Physics of Mirror Machines," a handbook under preparation at Lawrence Livermore Laboratory. The abstract is reproduced in its entirety here; it may appear in edited form in the handbook.)

The low frequency stability of strong ion rings and axisymmetric field reversed mirror plasmas is being studied, using time-dependent computer simulation methods. The techniques employed are applicable over a wide range of parameters, from the large-orbit field reversed ion ring (which might be used to confine additional dense, less energetic fusion plasma as conceived of for the Astron device), through FRM plasmas with $R_p/a_i \sim 5$, reversed-field theta pinch plasmas, and spheromak plasmas having much smaller nominal ion gyroradii. The effort has, until recently, been concentrated on ion ring configurations with $R_p/a_i \gtrsim 1$ and having a dense cold background plasma component. Present work is on creating appropriate FRM equilibria with $R_p/a_i \gtrsim 2$ for stability studies.

The simulation program is a linearized three dimensional hybrid code called "RINGHYBRID" (FRIEDMAN, SUDAN, and DENAVIT 1978,1979). This program models an ion ring (represented by particles) in a plasma consisting of a cold, uniform background ion component and an inertialess electron component of density appropriate for local

quasineutrality (both modeled by fluid equations). Since the background plasma components are assumed to be pressureless, the only zero order current is due to the ring ion component. To lowest order the ring particles (or the hot ions in an FRM run) are axisymmetric rings having r,z coordinates and r,θ,z velocities. First order perturbations having azimuthal mode number ℓ are considered, so that each particle k is deformed by an infinitesimal displacement $\underline{\xi}_k \exp(i\ell\theta)$. Fields and currents are represented by axisymmetric zero order parts, plus first order parts varying as $\exp(i\ell\theta)$, all defined on an Eulerian mesh in the r-z plane. Since each simulation particle represents a set of real particles lying on a nonaxisymmetric ring, a considerable economy of computation relative to a nonlinear 3d code is possible. Coupling between modes of different ℓ, nonlinear saturation, and other large-amplitude effects cannot be investigated with the linearized simulation, which serves largely as a replacement for linear theory, since the latter is difficult for such complicated configurations.

A method of generating quiescent equilibria through the addition of a resistive relaxation term ($-\sigma_0 \partial A_\theta^0/\partial t$) to the zero order field equation has been developed (FRIEDMAN and SUDAN, 1978). Because of the chaotic self-field betatron motion (or bounce motion) of the hot ions, and their limited number in the simulations, only an approximate equilibrium is possible; the goal of the method is the minimization of fluctuations in the important macroscopic moments (especially the current density).

Code performance has been verified by studying the normal modes of the cold background plasma, which has been represented both as a fluid

and by discrete particles centered in cells and on cell edges (with zero-order velocities set to zero). A consistent boundary condition arises from setting the tangential components of the first-order electric field to zero at the walls; this necessarily implies a nonzero normal component of the plasma velocity at the wall in this geometry. Further code verification has included a study of plasma return currents across a magnetic field, in cylindrical geometry and with no center conductor (FRIEDMAN, SUDAN, and DENAVIT, 1979).

The stability of infinitely-long current layer equilibria has been examined (A. Friedman, in preparation). Both stable and unstable kink and precessional motion have been observed; the unstable $\ell = 1$ motion in a radially decreasing field can be identified with the MHD precession first noted by BERK and SUDAN (1971), and described in detail by LOVELACE (1979).

The stability of thin, weak rings (i.e., rings which are not encircled by field lines) has been studied. A new tilting instability of the weak ring - plasma system has been observed in the simulations. The mechanism is similar to that of the kink instability of a strong beam; however, unlike the strong ring case, the stability threshold is dependent upon the background density. A simple heuristic analytical model which contains the essence of this mode has been developed (A. Friedman, in preparation).

Effects of ergodic single-particle orbits are observed in many of our simulations (FRIEDMAN, 1979); due to the structural instability of particle trajectories, neighboring orbits diverge exponentially (and

noisily) with time. In the zero order motion, this effect leads only to a loss of left-right mirror symmetry. However, in the first order motion the associated "growth" due to single-particle instability can often be sufficiently rapid as to mask the collective modes which are the true objects of study (the rate of orbit separation depends strongly upon the details of the equilibrium; see FINN, 1979). Because of the finite number of simulation particles employed, the random phases of the individual growing displacements $\underline{\xi}_k$ cannot force macroscopic moments to be zero as they would in a true Vlasov plasma with an infinite number of particles. Similar effects have been observed in the crude FRM equilibria we have generated to date; this has been the major impediment to more rapid progress in this direction. This problem is also likely to occur in future applications of nonlinear codes to problems of linear stability if certain "quiet-start" loadings are used (i.e. particles on circles initially).

The stability properties of some field reversed ion ring equilibria have been examined (A. Friedman, in preparation). One moderately thick ion ring with aspect ratio of order 4:1, for which the single-particle instability was not excessively rapid, has been studied in detail. This equilibrium is stable to the MHD precession (ℓ = 1 radial mode) because a conducting wall is present at finite radius; kink mode behavior is observed to agree closely with predictions based upon the thin-ring theories of LOVELACE (1975) and SUDAN and ROSENBLUTH (1975). Specifically, the ℓ = 2 and 3 radial kink modes, and the ℓ = 1 and 2 axial modes, are the only ones which show rapid growth. Some evidence

for the possible existence of betatron-resonance instabilities (FINN and SUDAN, 1979) has been observed for larger values of ℓ. The study of thicker rings has proven difficult because the single-particle instability masks the expected (slower) growth.

The RINGA model, a 2d3v (axisymmetric) nonlinear code, was used earlier in studies of ion ring formation, equilibrium, and compression (FRIEDMAN et.al. 1977; MANKOFSKY et.al. 1978). The physics contained in this program is similar to that of the version of the SUPERLAYER code used for mirror studies, although the algorithms employed are almost entirely different. Companion runs using RINGA and SUPERLAYER have showed good agreement, thus verifying the performance of both codes.

Future applications of these simulations may concern ion kinetic (e.g. loss cone) instabilities which are present in the infinite plasma (BYERS et.al., 1978). However, the primary concern is with gross configurational instabilities (MHD-like kink, sausage, etc.) and with ion kinetic modes whose instability depends upon the detailed shape of the field reversed equilibrium, (e.g. betatron resonance or bounce resonance effects).

---

* This work has been carried out in collaboration with Profs. J. Denavit of Northwestern University and R. N. Sudan of Cornell University; more recently, the author has gained much from interaction with Dr. J. A. Byers of LLL. The author gratefully acknowledges the support of Prof. C. K. Birdsall (U.C. Berkeley).

REFERENCES

A. Friedman, R. L. Ferch, R. N. Sudan, and A. T. Drobot, "Numerical Simulation of Strong Proton Rings," Plasma Phys. 19, 1101 (1977).

A. Friedman and R. N. Sudan, "A Method for Improved Convergence to High-Beta Equilibria in Particle Simulations," Cornell University Lab. of Plasma Studies Rept. No. 237 (1978).

A. Mankofsky, A. Friedman, and R. N. Sudan, "Numerical Simulation of Injection and Resistive Trapping of Ion Rings," Cornell University Lab. of Plasma Studies Rept. No. 245 (1978, submitted to Plasma Phys.)

J. A. Byers, B. I. Cohen, W. C. Condit, and J. D. Hanson, "Hybrid Simulations of Quasineutral Phenomena in Magnetized Plasma," J. Comp. Phys. 27, 363 (1978).

A. Friedman, R. N. Sudan, and J. Denavit, "A Linearized 3-D Hybrid Code for Stability Studies of Axisymmetric Field-Reversed Equilibria," Proc. Eighth Conf. on Numerical Simulation of Plasmas, Paper No. PC-13, Lawrence Livermore Lab. Conf. Proc. No. CONF-780614 (1978).

A. Friedman, R. N. Sudan, and J. Denavit, "A Linearized 3-D Hybrid Code for Stability Studies of Field-Reversed Ion Rings," Cornell University Lab. of Plasma Studies Rept. No. 268 (1979, submitted to J. Comp. Phys.)

A. Friedman, "Ergodic Orbits in Particle Simulations of Strong Ion Rings," U. C. Berkeley Electronics Research Lab. Rept. No. UCB/ERL M79/41, (1979, to be submitted for publication.)

J. A. Byers, Y. Matsuda, J. Stewart, and A. Friedman, "Linearized Three - Dimensional Simulation Codes Applicable to Stability of Field Reversed Plasma Configurations," Proc. IEEE Int. Conf. on Plasma Science (1979).

J. M. Finn, "Stochastic Behavior of Particle Orbits in Field Reversed Geometries," Plasma Phys. 21, 405 (1979).

J. PULSAR SPARKING

Dr. W. M. Fawley

A great deal of progress was made in simulating the initial growth, saturation, and final states of electron-positron pair creation cascades (= sparking) in pulsar magnetospheres. In brief, it appears that sufficiently copious pair creation always shorts out background electric fields (i.e., those induced by the rotation of the pulsar magnetic field) and that charge of both signs will periodically be able to flow out through the light cylinder. For all initial conditions studied to date, the initial burst of pair creation turns itself off by shorting out electric fields all the way to the neutron star surface. The accelerating electric fields build up again only after the relativistically hot pair plasma becomes sufficiently rarified via expansion through the light cylinder that the plasma suffers what is essentially a dielectric breakdown. Due to transit time effects, the pair creation rate then oscillates about an equilibrium. It is not clear yet as to whether these oscillations fully clamp out to zero or whether a certain amplitude is maintained indefinitely. The oscillations have a time scale (10^{-6} to 10^{-5} seconds) suggestive of the microstructure observed in many radio pulsars. A more detailed report will be given in a later QPR.

K. DIGITAL FILTERING IN TIME

Dr. W. M. Fawley (Prof. C. K. Birdsall)

We have made some progress in developing time filtering algorithms and give a short report here. A more detailed version will appear in a later QPR.

Following the ideas of Denavit et al., we have employed a backward-biased electric field in the acceleration subroutine of the 1-d electrostatic code ES1. However, we used a somewhat different biasing scheme. Using

$$\frac{V^{N+\frac{1}{2}}-V^{N-\frac{1}{2}}}{\Delta t} = \frac{q}{m}\left(\frac{(1+\varepsilon)}{2} E^{N+1} + \frac{(1-\varepsilon)}{2} E^{N-1}\right) \quad , \tag{1}$$

requires a predictor-corrector scheme to determine E^{N+1} which we prefer to avoid. Instead we found that substituting

$$\frac{q}{m}\left(\frac{(1+\varepsilon)}{2} E^{N+1/M} + \frac{(1-\varepsilon)}{2} E^{N-1/M}\right) \tag{2}$$

for the right hand side of Eq. (1) for $M > 1$ reproduced all the useful damping characteristics of the original equation. For sufficiently large M (we used $M=5$ and $\varepsilon=0.5$ in most runs), it is not necessary to use a predictor-corrector to determine $E^{N\pm1/M}$ inasmuch as one may advance $V^{N-\frac{1}{2}}$ to V^{N} using E^{N} and E^{N-1}, and then fairly accurately predict $X^{N\pm1/M}$ and thus $E^{N\pm1/M}$. Computationally, this method is somewhat faster than a predictor-corrector with only one correction step and is <u>much</u> faster if convergence of the predictor-corrector scheme requires more than one iteration.

We have tested a version of ES1 employing Eq. (2) on cold plasma oscillations and find that for $\omega_p \Delta t<2$, the algorithm is stable and that the damping rate increases quadratically with oscillation frequency. The algorithm is not generally stable for $\omega_p \Delta t>2$, though a "hybrid" version using many short time steps followed by a single, moderately long time step is stable for some parameters regimes.

The damping algorithm also appears to inhibit the growth rate of the multibeam instability at low spatial mode numbers, but it does not suppress the instability at higher mode numbers. We plan to investigate this problem further with Y. J. Chen.

L. NONPHYSICAL BEHAVIOR OF HYBRID OSCILLATIONS DUE TO ALIASING

Vincent Thomas (Prof. C. K. Birdsall)

While simulating hybrid oscillations of a cold plasma excited at large $k\Delta x$, large variations in the total energy were observed. These variations were due to an overall variation in the kinetic energy; there was no overall change in the electrostatic energy during the simulations. Moreover, the field energy was contained entirely in the mode initially excited. These characteristics are shown in Figs. 1, a through e. All figures are from simulations with the following parameters unless otherwise noted:

$$L = 32 \qquad \omega_p = 1 \qquad \text{MODE} = 14$$
$$NG = 32 \qquad \omega_c = 3 \qquad x_1(0) = \text{E-06}$$
$$v_y(0) = -\omega_c x_1(0) \quad .$$

The growth in the kinetic energy was imperceptible when the lower modes were excited, but increased monotonically to become many times the initial kinetic energy when the higher modes were excited initially (Fig. 2). The frequency of the kinetic energy variation (beat frequency) changed gradually from approximately 0.1 of the hybrid frequency for modes where the growth has just become noticeable to less than 0.01 of the hybrid frequency for higher modes. This beat frequency variation is fit well by the quantity $\omega_p^2/2\omega_H$ (Fig. 3). The plasma frequency and the hybrid frequency are taken to be the mode dependent quantities in this expression.

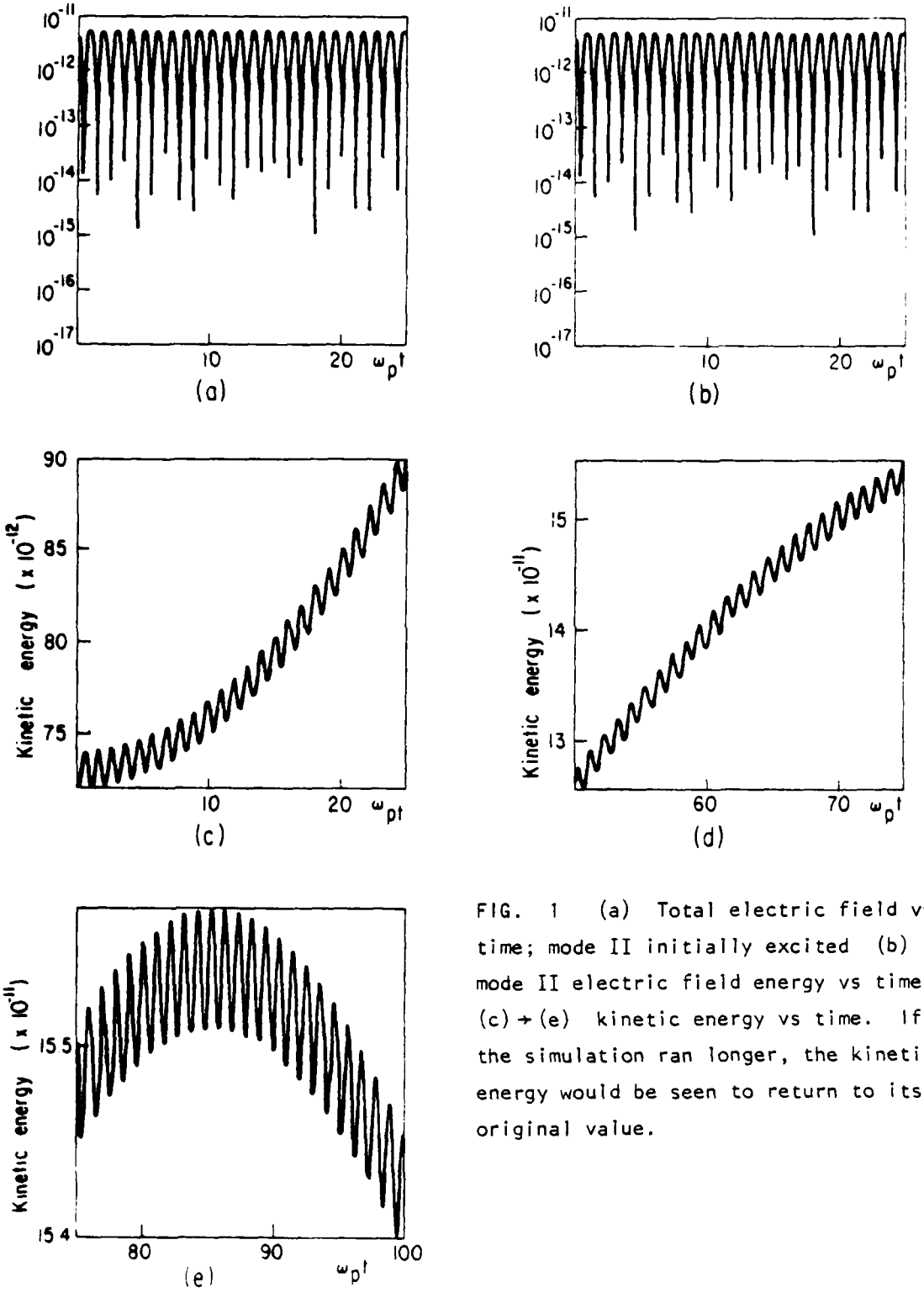

FIG. 1 (a) Total electric field vs time; mode II initially excited (b) mode II electric field energy vs time. (c) → (e) kinetic energy vs time. If the simulation ran longer, the kinetic energy would be seen to return to its original value.

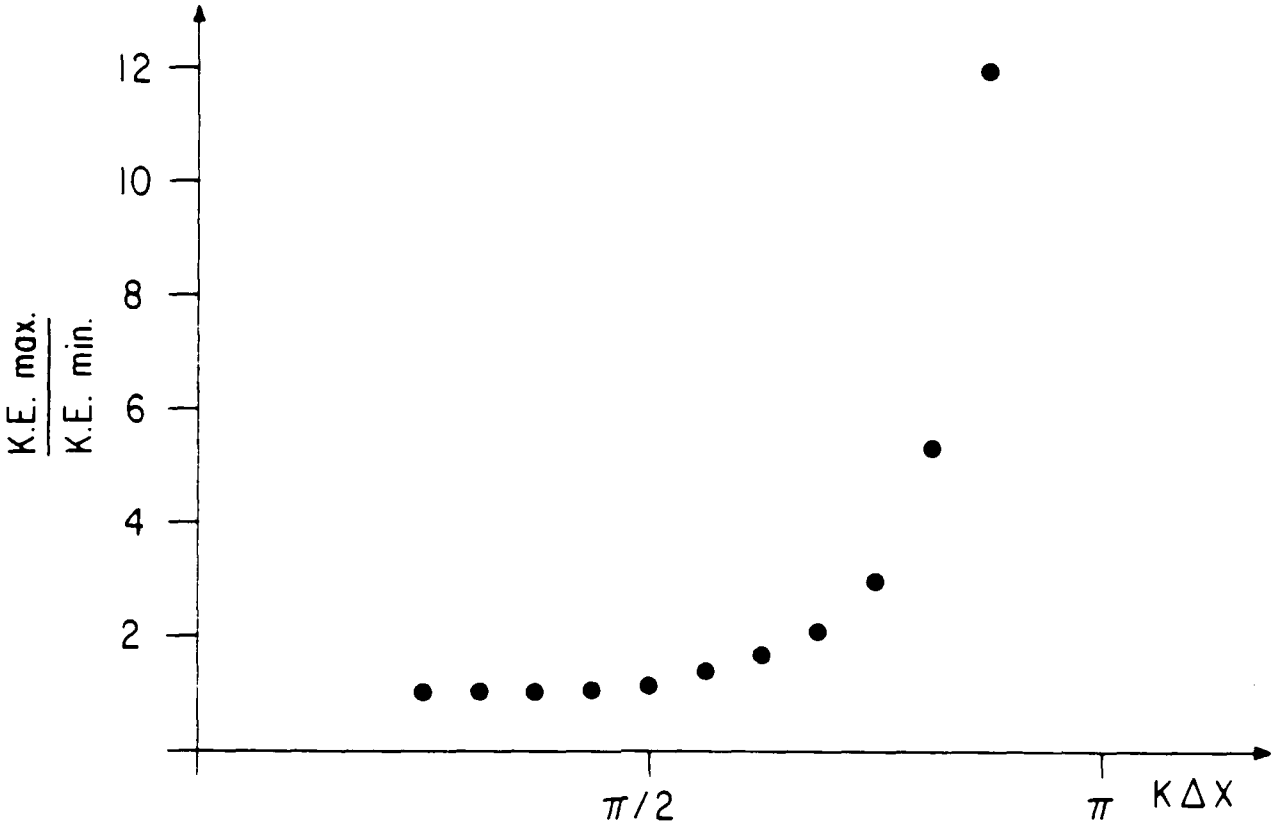

FIG. 2 The peak kinetic energy of the beat divided by the initial kinetic energy, as a function of kΔx, the mode initially excited (modes 4 through 14).

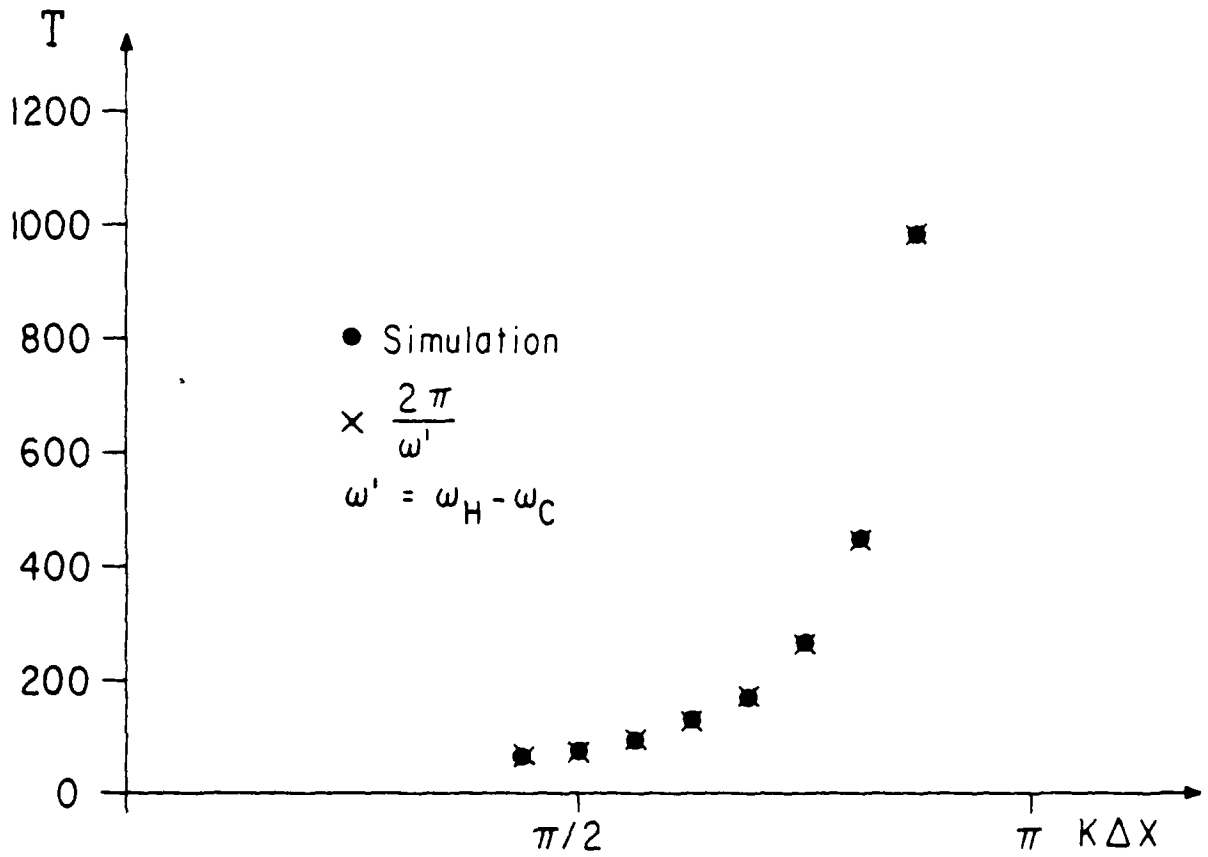

FIG. 3 The beat period T, for the kinetic energy vs kΔx. The crosses show the period for $\omega = \omega_H - \omega_c \approx \omega_p^2/2\omega_c$ the predicted value.

The total energy variations due to the kinetic energy variations were much less than the energy variations due to the overemphasis by the grid of the electrostatic energy for the first 6 modes of a 16 mode system. In this sense, the kinetic energy variation is not important for these modes.

Phase space plots showed generation of aliasing (Fig. 4). Plots of v_x vs. v_y displayed differences in phase that are not to be expected if the motion is that of anormal mode (Fig. 5). Histories of a single particle velocity space motion showed alternating growth and decrease with no drift (no E/B mistake) (Fig. 6). The simulation run for Fig. 6 was less than the period of an overall beat variation so that the particle is seen to be still spiralling outward. If the simulation was run longer, then the particle radius would seen to return to its original value. The particles showed different growth rates, with longest growth in positions where the amplitude of the electric field was largest.

When the time step was changed from $\omega_H\Delta t=0.15$ to $\omega_H\Delta t=1.5$, the amplitude and frequency of the energy variation changed only very slightly.

When the mode number was held constant and the number of grid points increased (meaning $k\Delta x$ decreased), the variations decreased, becoming negligible when enough grid points were added. "Enough" means that $k\Delta x<\pi/2$.

The nonphysical behavior remained for all excitations in $x_1(0)$ tried from 0.01 of a grid space (just a little less than the particle separation) to 10^{-6} of a grid space (which was approximately 10^{-4} of the particle separation. The frequency of the energy variation did not change when the excitation was varied and the relative amplitude remained the same.

ω_c was varied from 0.5 to 4 with the ω_p at 1. Increasing the cyclotron frequency yielded a larger amplitude and a longer period. Exhaustive studies were not done, but for all cases tried the frequency of the

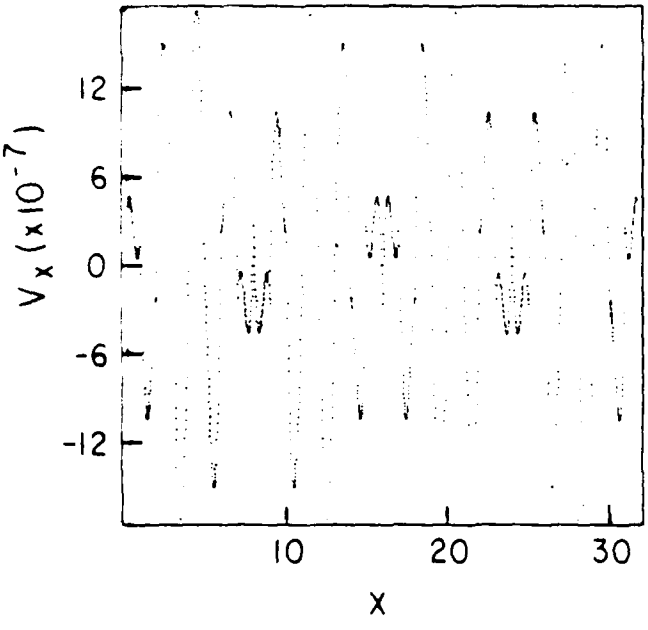

FIG. 4 v_x vs x at time = 50

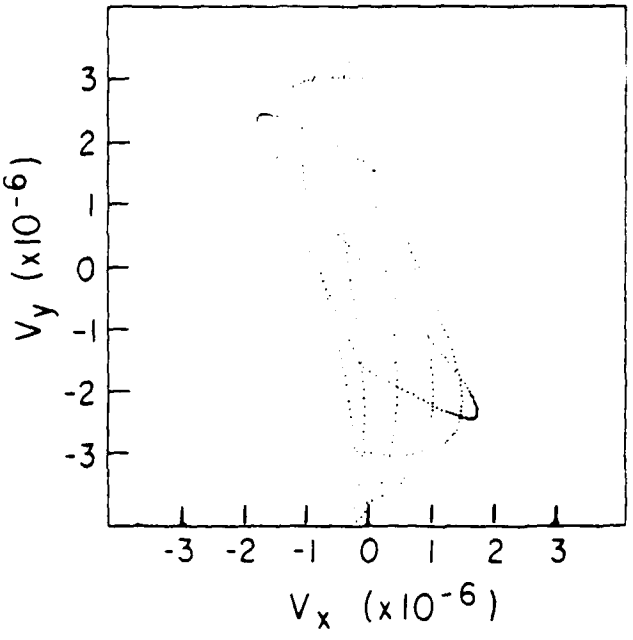

FIG. 5 v_y vs v_x at time = 50

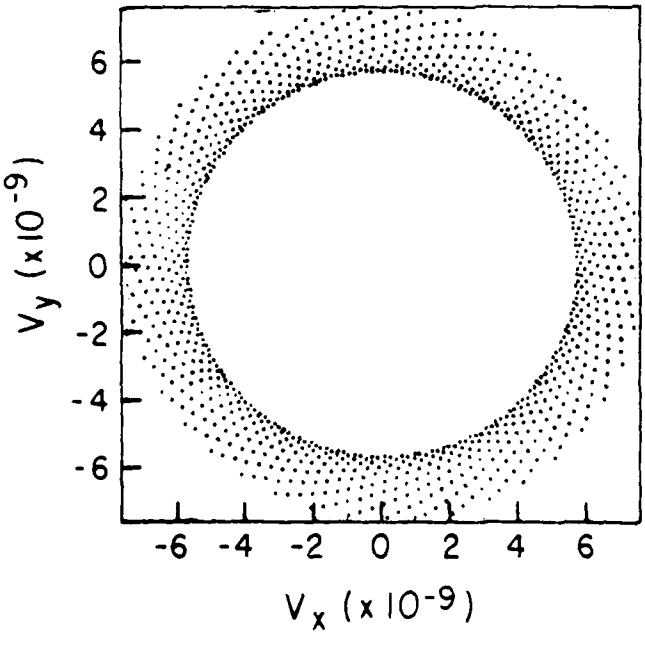

FIG. 7 v_y vs v_x for one particle from time = 0 to time = 50

variation was given by $\omega_H-\omega_c$. Through Fourier analysis of the kinetic energy, a high frequency component was also observed at $\omega_H+\omega_c$, which can be observed if $\omega_H+\omega_c$ is not much smaller than ω_H and so is separated from the peak at $2\omega_H$.

Changing the number of particles from 2048 to 256 did not change the relative amplitude of the variation.

In an attempt to investigate possible beating between the cyclotron frequency and the hybrid frequency (which would have a large period due to the decrease in the effective plasma frequency at high mode numbers), a simulation was done at mode 1 with a plasma frequency corresponding to the effective plasma frequency of mode 14. No nonphysical results were observed which implies that the poor aliasing properties of the higher modes is essential for the generation of the nonphysical results.

One simulation was done by perturbing the x velocity only but the unphysical results still occurred.

The frequencies of the energy variations can be calculated by making use of the fact that the electric field is sinusoidal and does not change its amplitude. An essential feature of this calculation is that it depends upon the nonsinusoidality in space of the force (or electric field) at high mode numbers. A typical electric field and its Fourier transform (treating the electric fields as a continuous function, rather than a grid quantity) are shown in Figs. 7 and 8. For lower modes only the principle term would be present. The analysis follows.

The equations of motion for hybrid oscillations, with $\underline{B}=\hat{z}B_o$, are

$$\ddot{y} = -\omega_c\dot{x} \qquad (1)$$

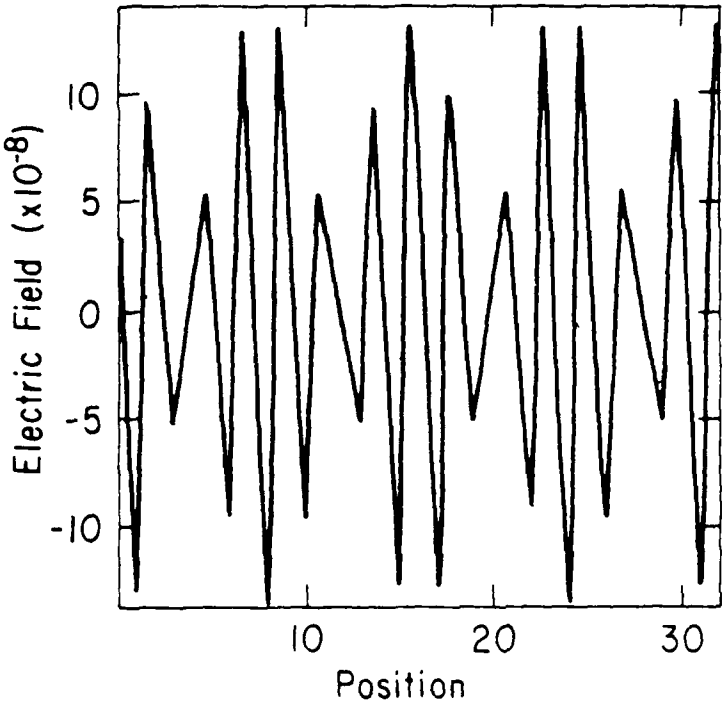

FIG. 7 Electric field at time zero. Note that NG = 32, mode 14 only excited kinetically (i.e., intial particle displacement and velocity) produces E at mode 14, plus other.

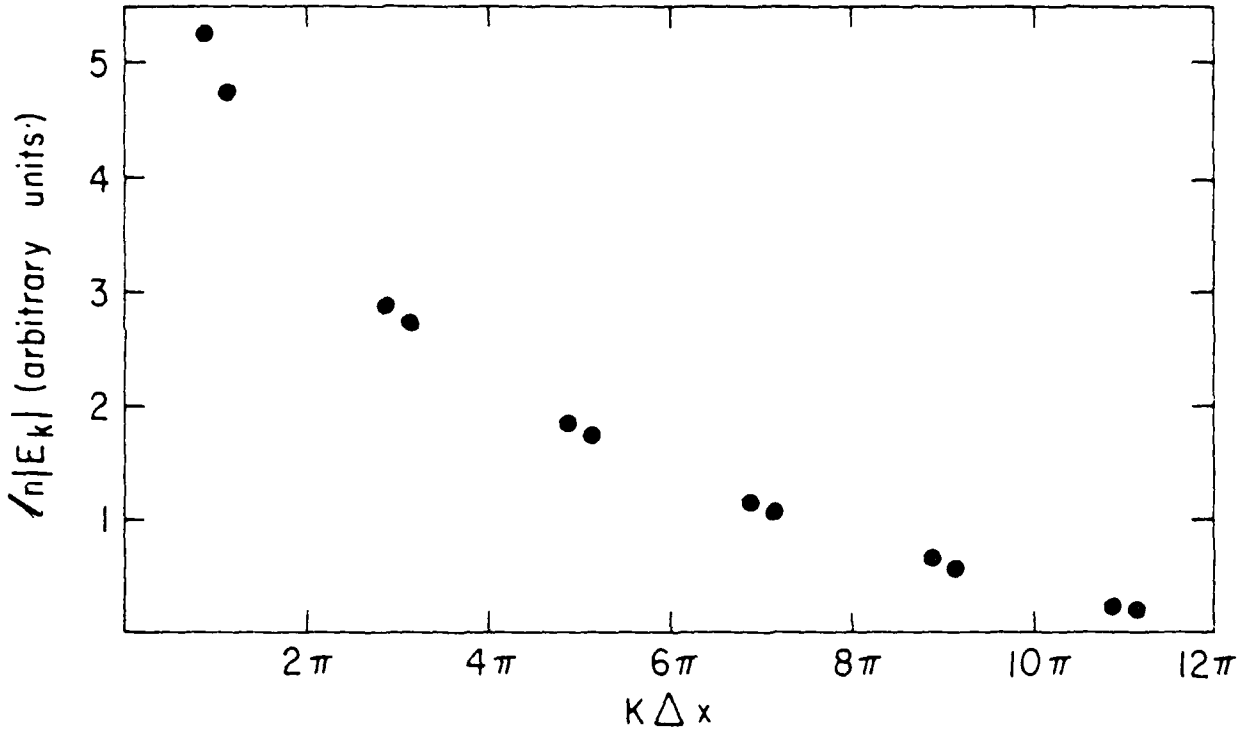

FIG. 8 The magnitude of the Fourier components of E obtained from E(x) of Fig. 7 using a very fine grid NG = 2048. The principal term near 3 corresponds to mode 14, the others are spatial harmonics which fold into mode 14, e.g., 18 (not seen).

$$\ddot{x} = \frac{qE}{m} + \omega_c \dot{y} \quad . \tag{2}$$

Integrating Eq. (1) with the special initial conditions of $\dot{y}(0)=-\omega_c x(0)$ and $\dot{x}(0)=0$ gives

$$\dot{y} = -\omega_c x \quad . \tag{3}$$

Putting Eq. (3) into Eq. (2) yields

$$\ddot{x} + \omega_c^2 x = \frac{qE}{m} \quad . \tag{4}$$

Fourier transforming this equation in x yields.[1]

$$\ddot{x}_k + \omega_c^2 x_k = \frac{q\, S(-k)\, E(k,t)}{m} \quad . \tag{5}$$

Here k is to be treated as a continuous variable, going from 1 to ∞. Note that the r.h.s. is <u>not</u> replaced by $-\omega_p^2 x_k$. From the simulations, we have observed that E(t) goes as $\cos(\omega_H t)$ where $\omega_H^2 = \omega_c^2 + \omega_p^2(k)$; therefore, we take

$$E(k,t) = A_k \cos \omega_H t \tag{6}$$

The most general solution to Eq. (5), using initial condition $\dot{x}_k(0)=0$, is

$$x_k(t) = C_1 \cos \omega_c t - q \frac{S(-k)\, A_k}{m\omega_p^2} \cos \omega_H t \tag{7}$$

For those modes which are <u>not</u> initially excited in displacement or velocity (but <u>are</u> excited in that an A_k exists), $x_k(0)=0$, $\dot{y}_k(0)=0$, we have

[1] See Chap. 8 in C. K. Birdsall and A. B. Langdon, <u>Plasma Physics via Computer Simulation</u>.

$$x_k(t) = -\frac{A_k\, q\, S(-k)}{m\omega_p^2}\left\{-\cos\,\omega_c t + \cos\,\omega_H t\right\} \quad . \tag{8}$$

The velocity components are $v_{xk}=\dot{x}_k$ and $v_{yk}=\dot{y}_k=-\omega_c x_k$ which produces

$$\begin{aligned}(KE)_k &= \frac{1}{2}m\,(v_{xk}^2 + v_{yk}^2) \\ &\sim 2\omega_c^2 + \frac{\omega_p^2}{2}\,(1 - \cos\,2\omega_H t) + \omega_c[(\omega_H-\omega_c)\,\cos\,(\omega_H+\omega_c)t \\ &\quad - (\omega_H+\omega_c)\,\cos\,(\omega_H-\omega_c)t] \quad .\end{aligned} \tag{9}$$

The high frequency at $2\omega_H$ is clearly seen and the low (beat) at $(\omega_H - \omega_c) \approx \omega_p^2/2\omega_c$ is clear; the frequency $(\omega_H+\omega_c)$ was also observed through Fourier analysis of the kinetic energy.

However, if we are sufficiently clever to excite x_k at t=0 so that $C_1=0$, that is, with proper normal mode amplitude

$$x_k(0) = -\frac{q\, S(-k)\, A_k}{m\omega_p^2} \quad , \tag{10}$$

then the solution is

$$x_k(t) = \frac{q\, S(-k)\, E(k)}{m\omega_p^2}\,\cos\,\omega_H t \tag{11}$$

with no beating; only one A_k is excited.

The point is that the force, F(x,t), seen by the particle (interpolated from the grid), is never purely sinusoidal. F(k,t)=S(-k)E(k) will contain more and more harmonics as the particle excitation is made at larger and larger $k\Delta x \to \pi$. For excitation at small $k\Delta x \ll \pi$, F(k,t) will contain essentially only the excitation wavenumber k; this will be

$$x_k(0) \approx - \frac{q\ S(-k)\ A_k}{m\omega_p^2} \qquad (12)$$

because

$$\frac{q\ S(-k)}{m} A_k \rightarrow \frac{q}{m}\ E(k) = - \omega_p^2 x$$

and

$$- \frac{-\omega_p^2}{\omega_p^2} = 1 .$$

A lesson from this exercise is that initial excitation at large $k\Delta x$ is highly undesirable, producing large alias fields and subsequent nonphysical beat motion. In addition, as plasmas excited at small wavenumber will, due to nonlinearities, excite modes at harmonic k's and also produce nonphysical beats, it is recommended that smoothing be used, probably for all modes $k\Delta x > \pi/2$.

Section II

CODE DEVELOPMENT and MAINTENANCE

A. ES1 CODE

(No special report this quarter)

B. EM1 CODE

(No special report this quarter)

C. EZOHAR CODE

(No special report this quarter)

D. ES1+EFL CODE

(No special report this quarter)

E. RINCHYBRID CODE

Alex Friedman

A new version of the user's manual for this code is available; this version contains a description of the functions of all code parameters and variables. To obtain a copy, type (on the CDC-7600):

```
FILEM RDS .CURRENT MANUAL / t v
NETOUT [usc] MANUAL ULC. BOX [nnn] MANUAL / t v
```

where [usc] is the user's location, and [nnn] the box number.

F. RADIAL SIMULATION CODE ES1RB

Niels Otani (Prof.C. K. Birdsall)

A radial plasma simulation code has been developed for the purpose of improving simulation methods in an r-θ coordinate system. Thus far, the code has been tested on simple plasma problems. These methods are intended to be useful in the study of a wide variety of problems including intrinsically radial problems in both the tokamak and magnetic mirror fusion machines and in other cylindrical devices, such as magnetrons.

Our code is a 1 ½-d (r,v_r,v_θ) code resembling in many respects the cartesian electrostatic code ES1, developed by A. B. Langdon (1970). However, our code operates without the grid used by ES1 on which charge density is accumulated and fields are calculated. Instead, particle accelerations are computed directly from particle-pair interactions. The main purpose for this is to study the effects of finite particle width independently of grid effects.

Particles used in this code are cylindrical shells with finite thickness with shape characterized by

$$S(r,r_i) = \begin{cases} \frac{\lambda}{w} & \text{for} \quad r_i < r < r_i + w \\ 0 & \text{otherwise} \end{cases}$$

where λ is the charge per unit length of the particle in the axial direction. $S(r,r_i)$ is the "radial profile" of a particle said to be at coordinate r_i and is defined by $S(r,r_i) = 2\pi r\rho_i(r)$. The charge density corresponding to this radial profile is shown in Fig. 1. As shown elsewhere in this QPR, this is the only particle radial profile which will conserve both energy

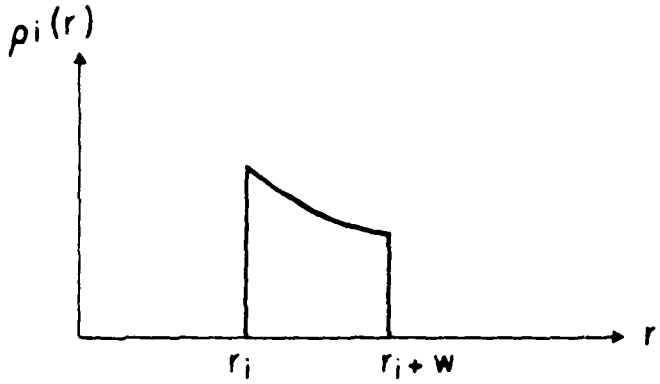

FIG. 1 Particle charge density as a function of radius.

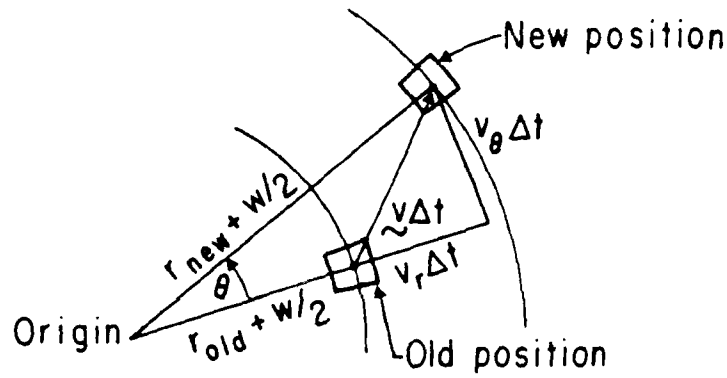

FIG. 2 Schematic illustration of ES1RB method of advancing particles.

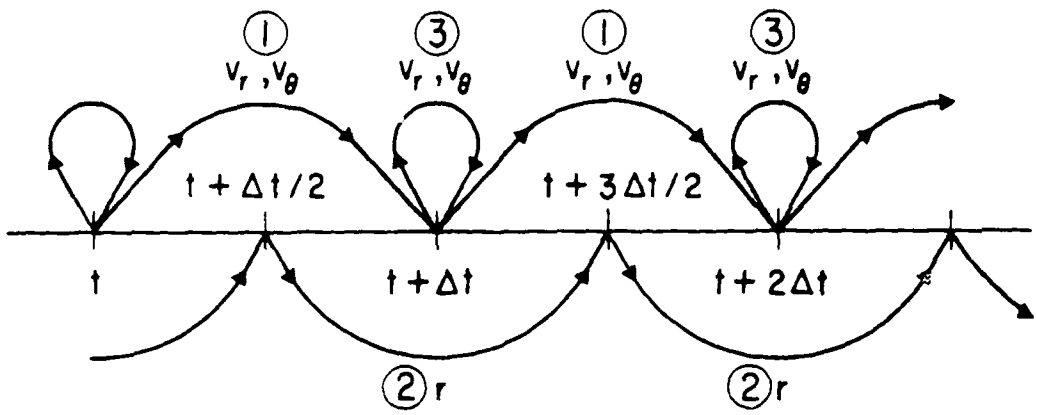

FIG. 3 Summary of the time centered leapfrog method used by ES1RB

(1) ½ - accel, rotation, ½ - accel

(2) radial coordinate mover

(3) velocity component mover

and momentum away from the origin in the limit $\Delta t \to 0$, and therefore is the natural choice for the particle shape.

The equations of motion to be simulated are

$$\dot{v}_r = \frac{v_\theta^2}{r} + \frac{1}{m}\int S(r)\, E_r(r)\, dr + \omega_c v_\theta \qquad (1a)$$

$$\dot{v}_\theta = -\frac{v_\theta v_r}{r} - \omega_c v_r \qquad (1b)$$

where, by Gauss' Law,

$$E(r) = \frac{2}{r}\sum_j \int_0^r S(r', r_j)\, dr' ,$$

m is the mass per unit length in the axial direction, and ω_c is the cyclotron frequency, $\lambda B_o/mc$. In other words, we consider only forces derived from a uniform external axial magnetic field, and from a self-consistent electric field, as in ES1.

The ACCEL routine of our code employs Langdon's half-acceleration-rotation-half-acceleration scheme modified for cylindrical coordinates:

$$v_{r1} = (v_r)_{old} + \frac{1}{m}\frac{\Delta t}{2}\int S(r)\, E_r(r)\, dr \qquad \text{(half-acceleration)} \quad (2a)$$

$$\left.\begin{aligned} v_{r2} &= v_{r1} + (\omega_c \Delta t)(v_\theta)_{old} \\ (v_\theta)_{new} &= (v_\theta)_{old} - (\omega_c \Delta t) v_{r1} \end{aligned}\right\} \qquad \text{(rotation)} \quad (2b)$$

$$(v_r)_{new} = v_{r2} + \frac{1}{m}\frac{\Delta t}{2}\int S(r)\, E_r(r)\, dr \quad . \qquad \text{(half-acceleration)} \quad (2c)$$

A time-centered leapfrog method of advancing particles is used: $(\underset{\sim}{v})_{old} = \underset{\sim}{v}(t)$, $(\underset{\sim}{v})_{new} = v(t+\Delta t)$, and $r = r(t+\Delta t/2)$. Provisions also exist in this portion of the code for adding velocity-proportional damping and uniform background charge.

The MOVER advances both the coordinate and the velocities to the new position according to the formulae:

$$r_{new} + \frac{w}{2} = \sqrt{\left(r_{old} + \frac{w}{2} + v_r \Delta t\right)^2 + \left(v_\theta \Delta t\right)^2} \tag{3a}$$

$$(v_r)_{new} = (v_r)_{old} \cos\theta + (v_\theta)_{old} \sin\theta \tag{3b}$$

$$(v_\theta)_{new} = -(v_r)_{old} \sin\theta + (v_\theta)_{old} \cos\theta \tag{3c}$$

where

$$\cos\theta = \frac{v_\theta \Delta t}{r_{new} + w/2} \tag{3d}$$

$$\sin\theta = \frac{r_{old} + w/2 + v_\theta \Delta t}{r_{new} + w/2} \quad . \tag{3e}$$

These relations are derived from the schematic illustrated in Fig. 2. We wish to have the center of mass of each angular section of the cylindrical particle moving according to Eq. (1). As is evident from Fig. 2, the center of mass coordinate, $r + w/2$, changes according to (3a), and the components of velocity vector $\underset{\sim}{v}$ are rotated by angle θ, owing to the rotation of the coordinate system at the new position relative to the old. Note that the rotation does not advance $\underset{\sim}{v}$ in time. It is however equivalent to the $-v_\theta v_r/r$ term in

Eq. (1b), and the centrifugal force term in Eq. (1a). The steps involved in advancing the particles are summarized in Fig. 3.

Initialization of the particles is achieved by means of an input file containing r, v_r, and v_θ values of all the particles. Pre-processor programs have been developed to generate these input files. This method of loading particles allows a great deal of flexibility with a minimum amount of effort. For instance, a simple method for establishing a one-dimensional radial equilibrium is to load the particles arbitrarily and use ES1RB itself with damping to damp the particles to equilibrium. ES1RB then produces a record of the equilibrium positions and this is used as the input file for the pre-processor, which can modify the equilibrium in whatever way desired. The modified file is then accepted as an input file by ES1RB for the main run.

To start the leapfrog scheme a routine analogous to the ES1 SETV is called once immediately after the particles loaded. This routine performs an acceleration followed by a rotation backwards in time by an amount $\Delta t/2$, and thus provides the proper offset between position and velocities.

Some Results

The equilibria for all simulations run so far have been established by the damping method just described. This process is illustrated in Fig. 4. It was found that the desired equilibrium was most efficiently achieved using a two-stage damping scheme. The first stage used a decay constant of ω_p (the plasma frequency) while in the second stage, damping is reduced to $0.1\omega_p$.

Radial plasma osciallations were simulated quite nicely by establishing equilibrium in the presence of a uniform background charge distribution. This equilibrium was perturbed slightly and used as the initial configur-

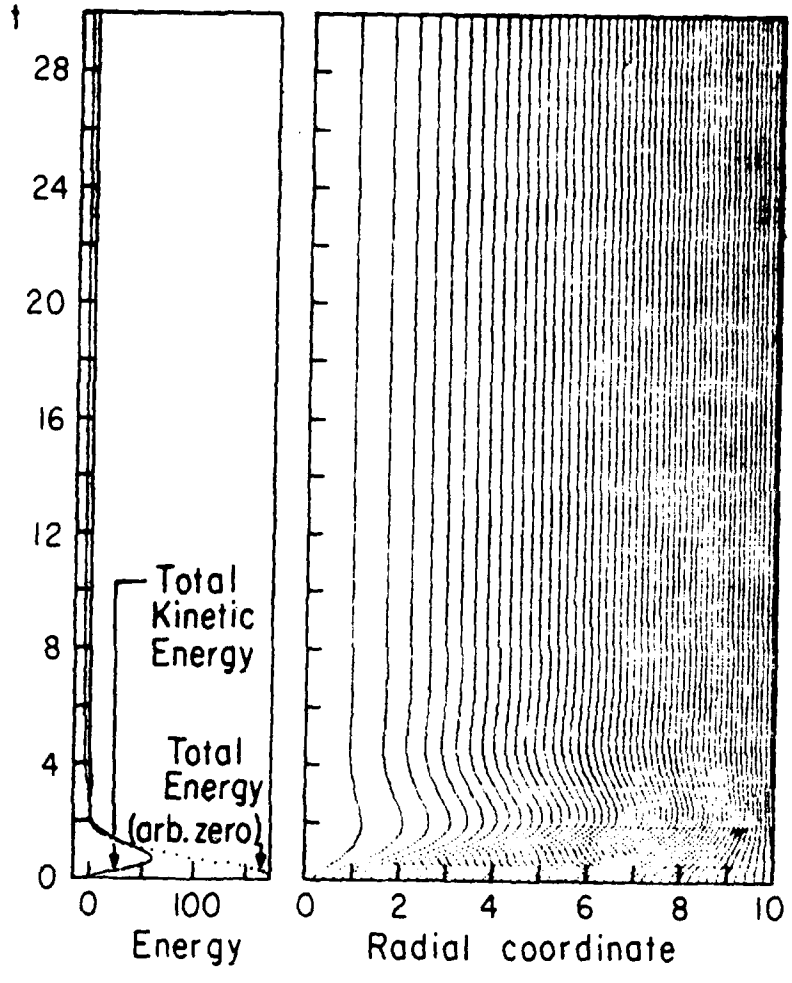

FIG. 4 Equilibrium for the main run is established using this preliminary damping stage. Only one stage was needed for thie particular run. Number of particles = 50, $2\pi/\omega_p = 4.42$, damping constant = $1.0\omega_p$, width of particles = 0.05.

ation for the main run. The result is shown in Fig. 5. The Fourier spectrum of the kinetic energy peaks quite sharply at $2\omega_p$, as expected. We also find that the use of wider particles and larger perturbations produces a more complicated kinetic energy spectrum, for reasons not yet completely understood.

Using a similar method, hybrid oscillations were also simulated (Fig. 6). The kinetic energy spectrum shows components at ω_p as well as $2\omega_p$. This was found to be a result of the initialization of all particles with $v_\theta = 0$. This leads to a superposition of a $\underset{\sim}{E} \times \underset{\sim}{B}$ drift on the hybrid oscillation motion of the particles. A calculation taking this $\underset{\sim}{E} \times \underset{\sim}{B}$ drift into account quantitatively agrees with the relative amplitudes of the ω_p and $2\omega_p$ Fourier peaks of 4 to 1 found computationally.

We have also found that the code accurately reproduces the equilibrium configurations of a completely non-neutral plasma column in the presence of an axial magnetic field as described in Davidson's Theory of Non-Neutral Plasmas, Ch. 1.

At the present time a study is being made of the possibility of the presence of a two-stream instability in the magnetic insulation sheath surrounding a cylindrical cathode.[1]

Of considerable concern in this project is the fact that an adequate method of dealing with the passage of particles through the origin has not yet been developed. As suggested in another article in this QPR, accurate (i.e., energy conserving) methods of simulating particle motion through the origin may not be easy to come by.

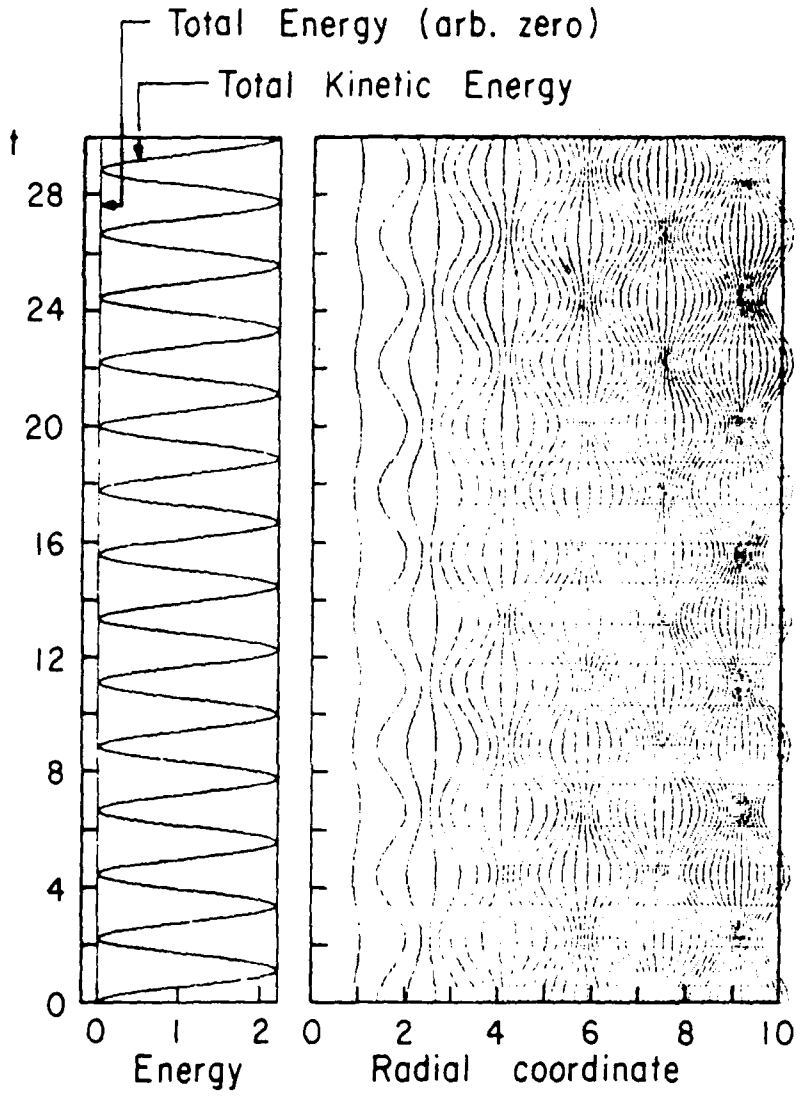

FIG. 5 Plasma oscillations using the equilibrium established by the run illustrated in Fig. 4. Note the agreement in the plasma period (theoretical $2\pi/\omega_p = 4.42$).

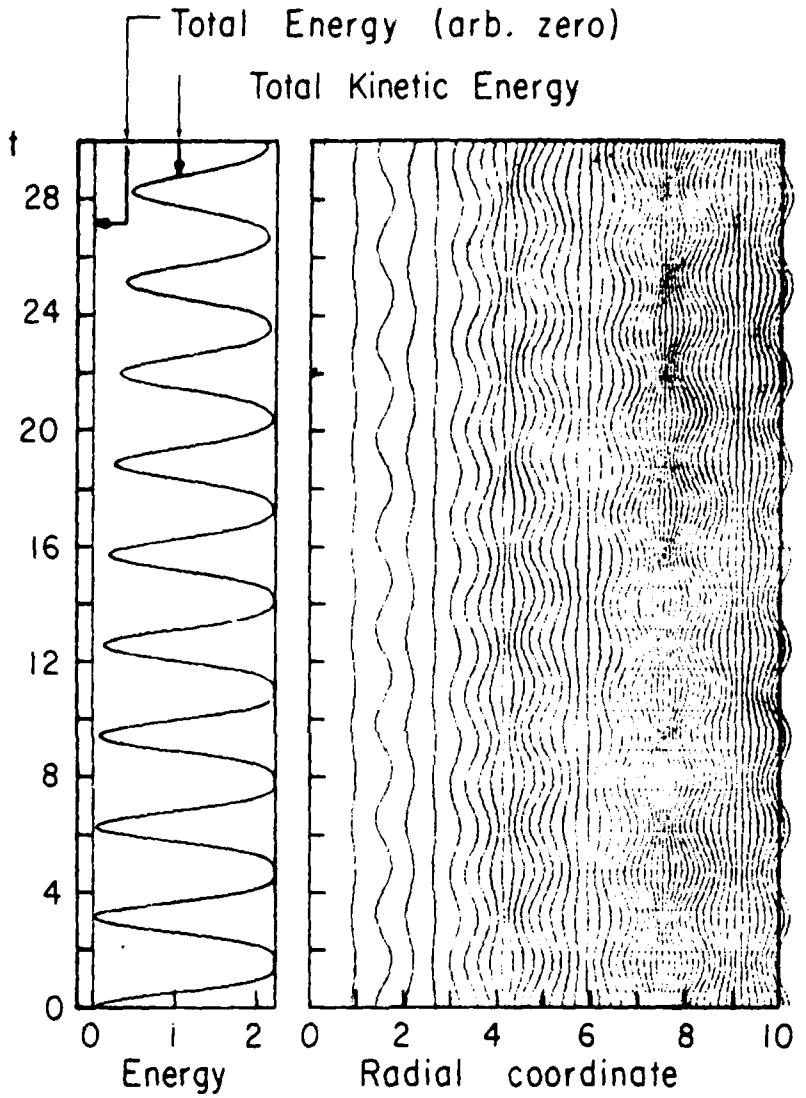

FIG. 6 Simulation of hybrid oscillations with superimposed $\underline{E} \times \underline{B}$ drift. Number of particles = 50, $\omega_c = \omega_p = 1.414$.

SUMMARY

Work on the problems involved in radial plasma simulation is continuing. So far we have limited projects to the simulation of known results and have met with moderate success. Some difficulties involving the passage of particles through the origin have been encountered. In the future, the code will be expanded to either a gridded 2-d, r-θ code, or to a $1\frac{1}{2}$-d gridded code employing a Fourier transform method[2] in θ to simulate a 2-d code.

REFERENCES

1. Lovelace, R. V., Ott, E., "Theory of Magnetic Insulation", Phys. Fluids 17, June 1974, p 1263.

2. Cheng, C. Z., Okuda, H., "New Three-Dimensional Simulation Models for Cylindrical and Toroidal Plasmas", J. Comp. Phys. 25, Oct. 1977, p 133.

G. CONDITION ON PARTICLE SHAPES IN 1D RADIAL CODES

Niels Otani (Prof. C. K. Birdsall)

A simple analysis shows that, away from the origin, only particles with $S(r,r_i)=S(r-r_i)$ can simultaneously conserve energy and momentum in the limit $\Delta t \to 0$. (Here $S(r,r_i)$ is defined by $S(r,r_k)=2\pi\rho_i(r)$ for a particle located at r_i.) If particles are forced to pass through the origin, energy conservation is impossible.

For energy to be conserved, we require

$$\frac{dK}{dt} + \frac{dU}{dt} = 0 \tag{1}$$

where K is the total kinetic energy:

$$K = \sum_i \tfrac{1}{2} m v_i^2 \tag{2}$$

in which v_i is the radial velocity of the i-th particle, and U is the total electrostatic potential energy:

$$U = \int_0^\infty 2\pi r dr \, \frac{E_r^2(r)}{8\pi} \tag{3}$$

It is understood that we are working in cylindrical coordinates and that all extrinsic quantities are per unit length in the axial direction. We assume that the electric field is due to the presence of all the charged particles and to a fixed background charge distribution. Thus, from Gauss' Law,

$$E_r(r) = \frac{2}{r}\left[Q_b(r) + \int_0^r \sum_i S(r',r_j)\, dr'\right] \tag{4}$$

where $Q_b(r)$ is the background charge inside radius r. We find then that

$$\frac{dK}{dt} = \sum_i m v_i \frac{dv_i}{dt} = \sum_i v_i \int_0^\infty dr\ S(r,r_i)\ E_r(r)$$

$$= \int_0^\infty dr \left(\sum_i v_i\ S(r,r_i)\right) \frac{2}{r} \left(Q_b(r) + \int_0^r \sum_j S(r',r_j) dr'\right) \qquad (5)$$

while

$$\frac{dU}{dt} = \frac{1}{4} \int_0^\infty r\ dr\ 2E_r(r) \frac{dE_r}{dt}$$

$$= \int_0^\infty dr \frac{d}{dt} \left(\int_0^r \sum_i S(r',r_i)\ dr'\right) \frac{2}{r} \left(Q_b(r) + \int_0^r \sum_j S(r',r_j)\ dr'\right)$$

$$= \int_0^\infty dr \left(\sum_i \frac{dr_i}{dt} \int_0^r \frac{\partial S}{\partial r_i} (r',r_i)\ dr'\right) \frac{2}{r} \left((Q_b(r) + \int_0^r \sum_j S(r',r_j)\ dr'\right). \qquad (6)$$

For all practical purposes, this necessitates

$$\frac{dr_i}{dt} \int_0^r \frac{\partial S}{\partial r_i} (r',r_i)\ dr' = - v_i\ S(r,r_i) \qquad (7)$$

using Eqs. (5) and (6) in Eq. (1). In the most general case, we need not have $dr_i/dt = v_i$, indeed, a mover using an algorithm of the form

$$f((r_i)_{new}) = f((r_i)_{old}) + v_i \Delta t$$

is conceivable. In the limit $\Delta t \to 0$, we then have $v_i = \frac{df}{dr_i} \frac{dr_i}{dt}$. Allowing

for this possibility, we see Eq. (7) is equivalent to

$$\frac{\partial S}{\partial r_i}(r,r_i) = -\frac{df}{dr_i}\frac{\partial S}{\partial r}(r,r_i) \tag{8a}$$

and

$$S(r=0,r_i) = 0 . \tag{8b}$$

If $f(r_i) = r_i$, then (8a) is equivalent to

$$S(r,r_i) = S(r-r_i) . \tag{8a'}$$

In other words, if energy is to be conserved, the radial profile S must be rigid and cannot change shape as the particle moves in and out. Clearly, such a restriction is incompatible with Eq. (8b) when particles pass *through the origin*; therefore energy conservation is impossible in any 1-d radial system in which particles pass through the origin.

A similar calculation can be done in the spherical case; here we find the same theorem true when the radial profile S is defined by

$$S(r,r_i) = 4\pi r^2 \rho_i(r) . \tag{9}$$

H. RADIAL CODE NOTES (R, Rθ, RZ, RθZ)

1. *INTRODUCTION* (C. K. Birdsall)

Simulations using radial coordinates or grids pose a number of problems for which some solutions will be presented. The problems and solutions to be presented are not claimed to be new or unique or exhaustive. The object is to gather together in this and succeeding QPR's some of the problems, solutions, and experiences with radial simulations.

Radial coordinates may be preferable to rectangular in 1d simulations using cylindrical and spherical R only, in 2d (cylindrical with Rθ or RZ, and spherical with Rθ, RΦ, θΦ) and in 3d (cylindrical with RθZ, spherical with RθΦ).

An object of using radial coordinates or grids is to emphasize radial behavior, usually implying that the physical and simulation models have a definite origin (R=0). There may be strong radial forces and motion or radial (circular or spherical) boundary conditions such that circular or spherical harmonics are more easily identified. Radial coordinate use is also promoted by the concern that using a rectangular mesh with rectangular boundaries will introduce unwanted moments in the grid quantities. This argument may hold for XY contrasted with Rθ, but not for XY contrasted with RZ. However, some conventional wisdom argues against abandoning rectangular meshes, pointing out that with XY meshes, problems with the origin are obviated, the equations of motion are more easily handled, the radial boundary conditions can be handled to good approximation and the circular harmonics diagnostics are obtainable to good approximation. Preferences, we think,

will be made easier and more rational by displaying the details of using radial coordinates and meshes.

The QPR radial code reporting comes from several sources, identified section by section.

2. ONE DIMENSIONAL MODELS (C. K. Birdsall)

One dimensional radial coordinates or meshes are clearly of general interest and eminently useful. An example is the set of electrostatic plasma diode problems solved by Barnes.[1] Let all of the charges be cylindrical shells (spherical shells can be done by inference) which move radially due to radial electric forces. The electric field within the s^{th} shell at r_s (see Fig. 1) may be obtained directly from Gauss' Law,

$$\int_{r\leq r_s} \rho \, dV = \int_{r_s} \underline{D}\cdot d\underline{S} \, . \tag{1}$$

The electric force on the s^{th} shell is dependent only on the net charge within that shell. The radial force on the s^{th} shell of uniform charge density ρ, line density $\rho_\ell = \pi\rho(b^2-a^2)$ due to all other charges is

$$F_r = \int_{shell} \rho E_r \, dV \, . \tag{2}$$

Specifically, the radial force on Shell I due to Shell II is (for uniform density shells)

$$F_{rI} \equiv \int_S \rho_I E_{rII} \, dV = \int_S \rho_I \frac{\rho_{\ell II}}{2\pi\epsilon r} \, 2\pi r \, dr \, dz$$

---

[1] Christopher W. Barnes, "The Computer Simulation of a Spherically Symmetric Plasma", SUIPR Report No. 344, Inst. for Plasma Research, Stanford Univ., March 1970.

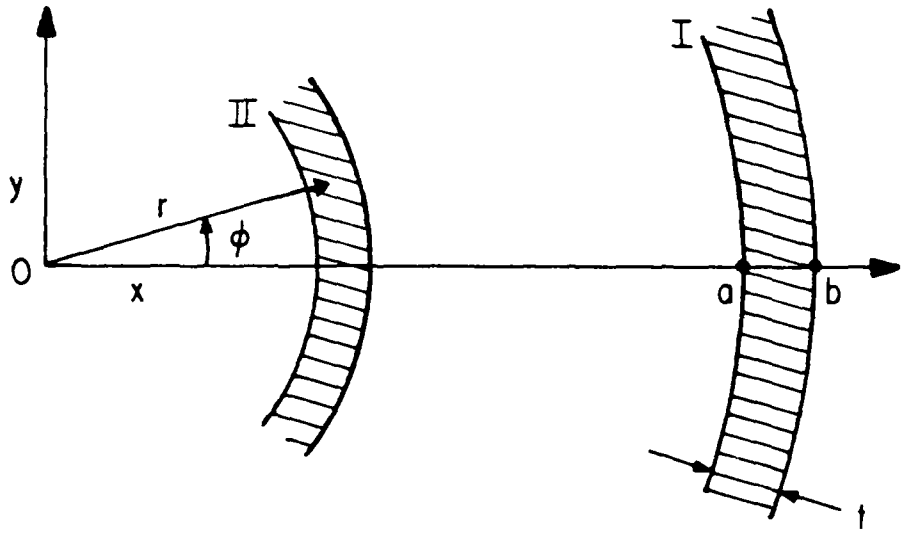

FIG. 1 Radial shells of charge.

$$= \frac{\rho_{\ell I}\, \rho_{\ell II}}{2\pi\varepsilon r_s}\, dz \qquad (3)$$

using

$$\rho_I (b-a) = \left[\frac{\rho_I (b-a)(b+a)\,\pi}{2\,\frac{(b+a)}{2}\,\pi} \right]$$

where

$$r_s \equiv \frac{a+b}{2} \quad .$$

That is, when Shell II is wholly inside of Shell I, then the force due to Shell II acts as if applied at the geometric middle of Shell I, independent of shell thickness.

The self force on Shell I, due to Shell I (after some algebra), is

$$F_{r_{self}} \equiv \int \rho_I\, E_{rI}\, dV$$

$$= \frac{\rho_{\ell I}^2}{2\pi\varepsilon r_s} \left(\frac{a + t/3}{2r_s} \right) dz \;\rightarrow\; \frac{1}{2} \left(\frac{\rho_{\ell I}^2}{2\pi\varepsilon r_s} \right) dz \quad \text{for } t \ll a \sim b \sim r_s \qquad (4)$$

This force is always radially outward; this effect is not found in planar slab models.

Let the shell be placed in a uniform background density of value ρ_b, opposite in sign, so as to oppose the self-force, with inward force on a thin shell of

$$F_{in} = \rho_\ell \left(\frac{\rho_b r_s}{2\varepsilon} \right) dz \; . \qquad (5)$$

The self and background forces compete, as shown in Fig. 2, going to zero at $v_s = r_{equilibrium}$, obtained from

$$\rho_\ell \frac{\rho_b r_e}{2\varepsilon} dz = -\frac{1}{2}\left(\frac{\rho_\ell^2}{2\pi\varepsilon r_e}\right) dz$$

or

$$\pi r_e^2 \rho_b dz = -\frac{1}{2} \rho_\ell dz$$

or

(background charge enclosed) = (half of the shell charge)

The net force is

$$F_{net} = \frac{1}{2} \frac{\rho_\ell^2}{2\pi\varepsilon r_s} + \frac{\rho_\ell \rho_b r_s}{2\varepsilon}$$

$$= \frac{1}{2\varepsilon} \rho_\ell \rho_b \left(\frac{-r_e^2}{r_s} + r_s\right)$$

$$m_\ell \ddot{r}_s = \frac{\rho_\ell \rho_b}{2\varepsilon} \frac{(r_s + r_e)(r_s - r_e)}{r_s}$$

which reads

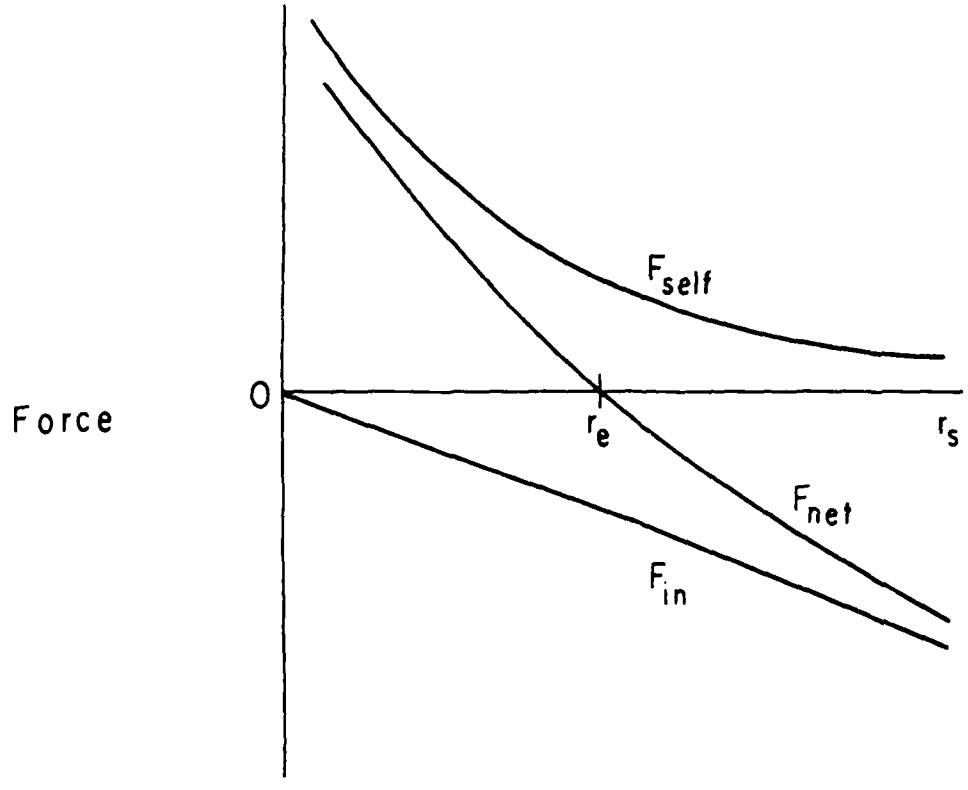

FIG. 2 Force acting on a thin shell at radius r_s, in a uniform background, tending to return the shell to equilibrium at r_e.

$$\ddot{r}_s = \left\{\left(\frac{\rho_\ell}{m_\ell}\right)\frac{\rho_b}{\varepsilon}\right\}\left(\frac{r_s + r_e}{2r_s}\right)(r_s - r_e) .$$

Using

$$\omega_p^2 \equiv -\frac{\rho_\ell}{m_\ell}\frac{\rho_b}{\varepsilon} \quad \text{(sign because } \rho_\ell\rho_b < 0\text{)}$$

then, for $r_s = r_e(1+\delta)$,

$$\ddot{\delta} = -\omega_p^2\,\delta\left(\frac{1+\delta/2}{1+\delta}\right) \approx -\omega_p^2\,\delta .$$

The motion is always oscillatory about r_e; it is simple harmonic only for $\delta \ll 1$ $|r_s - r_e| \ll r_e$. In contrast, a planar slab in a uniform background always has simple harmonic oscillations at ω_p.

3. *PARTICLE WEIGHTING TO GRID* (C. K. Birdsall)

Several methods for assigning particles to a radial grid will be given here. In all methods, the particles have coordinates r_i and charges q_i which are to be assigned to nearby grid points r_j. The particle shapes will fall out, with some differences from rectangular particles and grids; e.g., the shapes (or density profiles) may not be symmteric about a center, or, the average charge density of a particle will decrease as the charge (of fixed radial thickness) moves radially outward, or, the assignment at the origin may differ from that elsewhere, etc.

METHOD A (from B. I. Cohen, historical origin obscure)

The charge q_i is located at r_i between r_j and r_{j+1}, as

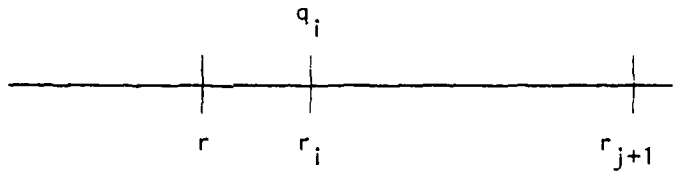

Let q_i be assigned to r_j, r_{j+1} by linear interpolation as derived from the charge density, which is

$$\rho_i \equiv q_i/(\text{volume of charge})$$

which, in cylindrical coordinates, for a cylindrical shell, is

$$= \frac{q_i}{(2\pi r_i \delta r \delta z)}$$

where $\delta r, \delta z$ are the nominal fixed dimensions of the charge. The density to be associated with r_j is linearly weighted from r_i, as

$$\rho(r_j) = \rho_i \left(\frac{r_{j+1} - r_i}{r_{j+1} - r_j} \right) = \rho_i \left(\frac{r_{j+1} - r_i}{\Delta r} \right)$$

where $\Delta r \equiv r_{j+1} - r_j$ and the density associated with r_{j+1} is

$$\rho(r_{j+1}) = \rho_i \left(\frac{r_i - r_j}{\Delta r} \right) .$$

However, charge is to be assigned, as follows:

$$q(r_j) = \rho(r_j)\, 2\pi r_j\, \delta r\, \delta z ,$$

$$q(r_{j+1}) = \rho(r_{j+1})\, 2\pi\, r_{j+1}\, \delta r\, \delta z$$

which is

$$q(r_j) = \left(\frac{r_j}{r_i}\right)\left(\frac{r_{j+1} - r_i}{\Delta r}\right) q_i$$

$$q(r_{j+1}) = \left(\frac{r_{j+1}}{r_i}\right)\left(\frac{r_i - r_j}{\Delta r}\ q_i\right) .$$

The check on charge conservation

$$q(r_j) + q(r_{j+1}) = q_i$$

is observed. Applying these weights produces $q(r_j)$ as a function of r_i as shown in Fig. 1.

A similar approach works in spherical coordinates with spherical shells, where

$$\rho_i \equiv \frac{q_i}{(4\pi r_i^2 \delta r)}$$

with assignment of density done quadratically, as

$$\rho(r_j) = \rho_i\left(\frac{r_{j+1}^2 - r_i^2}{r_{j+1}^2 - r_j^2}\right)$$

$$\rho(r_{j+1}) = \rho_i\left(\frac{r_i^2 - r_j^2}{r_{j+1}^2 - r_j^2}\right)$$

leading to

AD-A088 122 CALIFORNIA UNIV BERKELEY ELECTRONICS RESEARCH LAB F/G 20/9
PLASMA THEORY AND SIMULATION.(U)
SEP 79 C K BIRDSALL, A FRIEDMAN, W FAWLEY N00014-77-C-0578
UNCLASSIFIED NL

END
DATE FILMED
9-80
DTIC

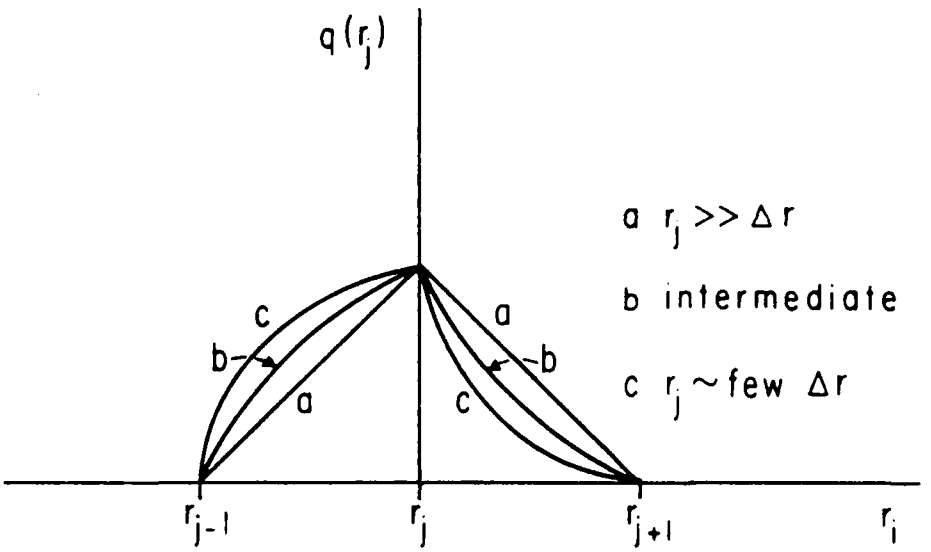

FIG. 1 Charge assigned to r_j as a function of charge position r_i. For $r_j \gg \Delta r$, the familiar planar linearly weighted triangular shape is seen. For r_j a few Δr, the shape is distorted, as shown.

$$q(r_j) = \left(\frac{r_j}{r_i}\right)^2 \left(\frac{r_{j+1} - r_i^2}{r_{j+1}^2 - r_j^2}\right) q_i$$

$$q(r_{j+1}) = \left(\frac{r_{j+1}}{r_i}\right)^2 \left(\frac{r_i^2 - r_j^2}{r_{j+1}^2 - r_j^2}\right) q_i$$

which also conserves charge, $q(r_j) + q(r_{j+1}) = q_i$.

I. RJET DEVELOPMENT

(No special report this quarter)

J. SOFTWARE DEVELOPMENTS

H. Stephen Au-Yeung

(1) FREX

FREX allows the user to extract selected frames from one or more FR80 graphic files on the CRAY into one FR80 output file. This program can be obtained by typing:

```
rfilem  read 1222 .cray frex(ESC)end  /  t v
```

This document corresponds to the FREX version of October 10, 1979. Later versions of FREX will be stored in FILEM directory .cray of user number 1222. The user should periodially check the date of this file (filem how 1222 .cray frex) to see if the program has been updated. The file FREX is a LIB file: it contains the latest sources as well as the latest documentation. To get the documentation, type:

```
lib frex(LF)x frex/doc(LF)end  /  t v
netout  [usc] frex/doc [swp.] box nnn frex  /  t v
```

The commands in FREX are similar to those in DDEX, a DD80 file frame extracting program that resides on the CDC-7600 (see LIBRIS #57). The following is a summary of all FREX commands:

⟨integer⟩ -
The frame (represented by the number ⟨integer⟩) to be extracted. (FREX allows only the second one of the two header frames to be extracted by the user: it is referred to as frame number 0. The first graphic frame is referred to as frame number 1, and so on.)

⟨integer⟩ thru ⟨integer⟩ -
"thru" can be replaced by "t" or "to". It causes all frames between the two integers, inclusive, to be extracted.

infile ⟨file name⟩ -
Change the input file. All selected frames of the previously opened file are extracted before opening the new one.

end,-
Terminate, processing all selected frames.

quit -
Like "end", but when entered after the "infile" command causes previously entered frames to be extracted without changing the input file or causing termination: more frame numbers can then be entered.

box ⟨nnn⟩ ⟨id⟩ -
The id string consists of up to 24 alphanumeric characters: embedded spaces may appear incorrectly and are not recommended: use the period or slash instead. The output file name is constructed from the id line: it is of

the form f0<first six characters of id>. If id consists of fewer than six characters, the filename is right-filled with asterisks to ensure an eigth-character file name. If the file to be generated exists, the user is given the option of overwriting it.

size <intger> -
To specify the size (in words) of the output file (defaults to 200000b). This command has to be issued before the box and id is entered; otherwise, the default size will be used.

family <the first file name of a file family> -
This is the same as the "infile" command except that when the end of file is encountered, FREX will open the next file within the family. All file names must be exactly 8 characters long. The last name in the family should end with an "x" (e.g. f105rp0x or f9test4x, etc.). The last two characters of other files must be numeric between "00" and "99".
Note: The BASELIB routine ZSEQHSPZ is used.

cancel <integer> -
Cancel the frame number <integer> that has previously entered for extraction (frame must be cancelled 1-by-1).

nochar -
Eliminate all alphanumeric characters from all frames. Useful for suppressing crowded labels on axes when preparing figures for publication.

char -
Reverse the effect of "nochar" (i.e. return to default mode).

offset <integer> -
Set offset for calculation of frame numbers (defaults to 0 and usually not required). For example, if the number 3 is entered, all frame numbers entered after this command will have 3 added to them before processing.

Restrictions:

(1) The routine will fail if the output exceeds the size specified by the "size" command.

Example 1:

This example shows how to extract frames from different FR80 files.

```
        user:  frex  size 400000b  box b22 solv  /  1 .2
routine/user:  /infile f104.a.1
routine/user:  /1
routine/user:  /infile f104.a.2
routine      :  Processing file:      f104.a.1
routine/user:  /1 2 3
routine/user:  /infile f104.b.1
routine      :  Processing file:      f104.a.2
routine/user:  /1 t 3
routine/user:  /end
routine      :  Processing file:      f104.b.1
routine      :   all done
```

The output file in this case will be "f0solv**".

Example 2:

One thing not mentioned above is that the first input file appearing on the execution line right after "frex" needs no "infile" command.

```
        user:  frex  f105rp0x  box b22 case1  /  1 .1
routine/user:  /b t 30
routine/user:  /cancel 15  cancel 21  end
routine      :  Processing file:      f105rp0x
routine      :   all done
```

This will cause frames 6-14, 16-20, and 22-30 to be extracted from the file "f105rp0x" and to be put into the file "f0case1*".

Example 3:

It is often best to input everything on the execution line (if possible).

```
        user:  frex  f105rq0x  1 t 4  box b22 x1-4(LF)end  /  1 .1
routine      :  Processing file:      f105rq0x
routine      :   all done
```

Example 4:

This shows how to obtain both frames with and without alphanumeric characters.

```
        user:  frex  f105rq0x  box b22 char+-  /  1 .1
routine/user:  /1 t 3  infile quit  nochar  1 t 3  end
routine      :  Processing file:      f105rq0x
routine      :  Processing file:      f105rq0x
routine      :   all done
```

In the output file "f0char+-", the first three frames are identical to those in "f105rq0x"; but all alphanumeric characters in frames 4 to 6 are eliminated.

Warning: some (maybe all) characters generated by DISSPLA are drawn and hence cannot be eliminated.

Example 5:

This is an example of having a file family as input.

```
        user:  frex  family f105ar01  box b22 ar/fam  /  1 .1
routine/user:  /1 t 500 end
routine      :  Processing file:     f105ar01
routine      :  Next file in family: f105ar02
routine      :  Last file in family: f105ar0x
routine      :  WARNING: INPUT FILE CONTAINS ONLY  242 FRAMES
routine      :   all done
```

The warning given above is to tell the user the number of frames extracted when reaching the end of file.

Acknowledgments

I would like to thank Maurie Manning (NMFECC) for providing information on the data format of FR80 files, and Alex Friedman for reviewing this documentation.

(2) COMOUT

Since NETOUT creates a header and a trailer for every file, it is desirable to combine several files into one before using NETOUT. COMOUT combines any number of files into one file; yet each file can have its own options. COMOUT is available on both the CRAY-1 and the CDC-7600. To get it, type:

(1) On the CRAY-1 -
```
rfilcom  read 1222 .cray  comout(LF)end  /  t v
```
(2) On the CDC-7600 -
```
rfilcom  read 1222 .say76 comout(LF)end  /  t v
```

This document corresponds to the COMOUT version of August 10, 1979. Later versions of COMOUT will be stored in FILEM directories .cray and .say76 (for CRAY and 7600 versions, respectively) of user number [illegible]. The user should periodically check the date of these files (filcom lbo 1222 .cray comout(LF)lbo 1222 .say76 comout) to see if the programs have been updated. The file COMOUT (on both machines) in a LIB file contains the latest sources as well as the latest version of this documentation. To obtain this document, type:
```
lib comout(LF)x comout/doc(LF)end  /  t v
netout (cos) comout/doc box bxx comout  /  t v
```

There are only two commands in COMOUT: they are:

globals: - The rest of the input line is assumed to be NETOUT options for the combined file. At most 5 options will be accepts. If "globals:" occurred more than once, the latter overrides the former.

end - Terminates COMOUT

Notes:

(1) Both commands have to be the first symbol of a input line.
(2) The user can enter as many lines as he/she wants. Each input line that does not contain a command has to be valid for NETOUT. Line feed and escape keys are not allowed. The prompt from COMOUT is ">".
(3) Destination (site) and box&id should be entered from input lines other than that global options are specified. Destination must be the first symbol of a input line, and box&id must be the last three symbols of a input line. If they are specified more than once, only the first one is taken.
(4) "globals:", destination, and box&id are all optional.
(5) On the 7600, the "C " option is specified for "globals:" internally. Any option specified under "globals:" that conflicts the "C." option is not allowed.

Example:
```
          user:  comout globals: uc.
  routine/user:  >como/doc box b22 comout
  routine/user:  )ucb endwith. /s s.
  routine/user:  )end
  routine      :  \comout\ : file id is comout    - rxucb/ka
  routine      :   all done
```

(3) DB

DB is a simple data base management system that uses a hashing mechanism to store and retrieve a record. DB is available on the CDC-7600 and can be obtained by typing:

```
filem  read 1222 .say76 db(LF)end  /  t v
```

This report corresponding to the DB version of October 2, 1979. Later version of DB will be stored in FILEM directory .say76 of user number 1222. The user should periodically check the date of this file (filem how 1222 .say76 db) to see if the program has been updated. The file DB is a LIB file; it contains the latest sources as well as the latest documentation. To obtain the documentation, type:

```
lib db(LF)x db/doc(LF)end  /  t v
netout  [use] db/doc ulc. [swp.] box nnn db  /  t v
```

a. The ACCESS option

The ACCESS option is used to create and/or to update the data base. It has the following syntax:

```
db access <new or old>=<data base file name>  /  t v
```

If NEW is specified, the user will be asked to define the data base. The following are the prompted messages and their meanings:

field name:	- Each record is composed by fields. A maximum of 20 fields is allowed. Each field name can have up to 50 characters or 5 words (with each word of less than 10 characters). Note that the first field is always used as the hash key; therefore the contents of that field has to be unique.
field length:	- The length in characters of the field. The maximum length allowed is 50 characters.
new field name:	- This will appear only if the last field name entered exists.

This process can be terminated by entering "end" to the prompt "field name:".

After the data base is defined, or if OLD is specified, the prompt ">" will appear and the user can then update the data base by using the following commands:

add <hash key>	- Add a record with the first field = <hash key>.
delete <hash key>	- Delete the record with the first field = <hash key>.
update <hash key>	- Update the record with the first field = <hash key>. To change the first field, the

```
                    user has to delete the whole record and add
                    a new one.  The user may hit only the return
                    key to those fields that remain unchanged.
  show <hash key>   - Print the record with the first field =
                    <hash key>.
  done              - Terminate DB.
```

Example:

```
          user:  db access now=friends
  routine/user:  field name:    name
  routine/user:  field length:  40
  routine/user:  field name:    phone number
  routine/user:  field length:  12
  routine/user:  field name:    street
  routine/user:  field length:  50
  routine/user:  field name:    city
  routine/user:  field length:  25
  routine/user:  field name:    state
  routine/user:  field length:  6
  routine/user:  field name:    zip
  routine/user:  field length:  5
  routine/user:  field name:    end
  routine/user:  >add Au-Yeung, H. Stephen
  routine/user:  phone number: 415-642-3477
  routine/user:  street:       International House
  routine/user:  city:         Berkeley
  routine/user:  state:        CA
  routine/user:  zip:          94720
  routine/user:  >done
  routine     :   all done
```

It is important to note that an upper case character is represented internally by three characters - 0@ plus the lower case character.

3. The PRINT option

To generate a list of the data base, one uses the PRINT option as follows:

```
  db print <data base file name> [output file name [site]]  /  t v
```

If the output file name is omitted, it defaults to "dbout.p". If site is given after the output file name, the output will be sent to the destination <site> by running the NETOUT program.

The user will then be asked the fields that he would like to be sorted. This should be entered from the highest priority to the lowest and terminated by entering "end".

Example:

```
          user:  db print friend friend.p
  routine/user:  field to be sorted: state
  routine/user:  field to be sorted: name
  routine/user:  field to be sorted: end
  routine     :              sort terminated normally
  routine     :   all done
```

(4) TIME

TIME allows any program (except TIME itself) to be run under its control. It prints the time used by the controllee when the controllee terminates. TIME is available on the CRAY-1 and can be obtained by typing:

```
rfilem read 1222 .cray time(LF)end  /  t v
```

This document corresponds to the TIME version of July 23, 1979. Later version of TIME will be stored in FILEM directory .cray of user number 1222. The user should periodically check the date of this file (filem how 1222 .cray time) to see if the program has been updated. The file TIME is a LIB file; it contains the latest sources as well as the latest documentation. To obtain the documentation, type:

```
lib time(LF)x time/doc(LF)end  /  t v
netout [usc] time/doc box bnn time  /  t v
```

There is only one command in TIME - fin, to terminate the program. The user can sequentially run as many programs (controllees) as he/she wishes. Before entering the name of the next controllee, the user should wait for the prompt ">>" to appear.

K. REPORT GENERATION

Alex Friedman

Recent developments have made report generation on the NMFECC computer facilities more convenient for users at sites serviced by mini-USC's, such as U.C. Berkeley. The first of these is the availability of the output options "nice" and "xnice" in the "PRINT" command of TRIX AC; these options send output to the NIPS printer with drawn type fonts. To find out more about them, obtain a copy of the latest RED report, as described in the previous OPR. Note that NIPS output arrives more promptly than high-quality hardcopy output, and is far less costly. Also note that plot files generated in any manner can be sent to the NIPS by use of utility routine "NIPIT", and so if the user prefers to invoke REDPP directly rather than through the TRIX PRINT command, this is possible.

The second development is the implementation of the "TURN." option of NETPLOT, the routine which is used to send graphics files to the local Versatec printer/plotter. This option is useful for all plotted output, as the plots are rotated by 90 degrees and so the user can leaf through the output in book form. However, it is particularly useful for plotting text, as one can now obtain output where the pages appear in "forward" order. The "ampersand zq" command to REDPP can be deleted. A sample COSMOS deck to perform the appropriate processing on the file "example" of the previous OPR is the revised file "swapexam", which contains:

```
*select p=swaprec
*netout ucb example s, ulc, box b34 example
*trix ac
*-red7
*-a
*-example
*-r11,2
*-#papersize 66 72 .94 .1 .32 0. 0.
*-.
*-nf(temp0)
*-format(temp0,temp1)
*-end
*redpp temp1 startp. 1 paperr. keep. defont. 2 2inits. &
*-filesize. 1350000 fr80brk. 1300000
*-box b34 example
*netplot ucb alwith. f0hcy fxhcy f. 1. turn. box b34 example
```

Section III
PLASMA SIMULATION TEXT

One publisher has manuscript for review, looking favorable. As this has dragged on (their problem), up-dating will be required, when and if accepted. We have been out of copies for months and do not plan to reprint, at present.

Section IV
SUMMARY of REPORTS, TALKS, PUBLICATIONS IN PAST QUARTER

Abstracts follow of papers submitted (this quarter) for Division of Plasma Physics Meeting, American Physical Society, Boston, Mass., Nov. 12-16, 1979 (next quarter).

Jae Koo Lee and C. K. Birdsall, "Velocity Space Ring-Plasma Instability, Magnetized, Part I: Theory, Part II: Simulation", Phys. Fl. 22, 7, pp. 1306-1314, 1315-1322, July, 1979.

H. Stephen Au-Yeung and Alex Friedman, "Solver: An Analytic Function Root Solving and Plotting Package", ERL Memo No. UCB/ERL M79/55, 31 August 1979.

Saturation of the Lower-Hybrid Drift Instability. YU-JIUAN CHEN and C.K. BIRDSALL, U.C. Berkeley*—The linear properties and the saturation mechanism of the lower-hybrid drift instability are studied using a 1D particle-hybrid simulation. The model is a slab with a constant density gradient; the ions are unmagnetized particles, shielded by the strongly magnetized electrons through the linear electron susceptibility, χ_e. Ions are initially in a steady equilibrium state with the ion diamagnetic drift velocity cancelled by the $\underline{E}\times\underline{B}$ drift, corresponding to electrostatically confined ions. At small amplitudes, the simulation shows good agreement with linear theory, such as the linear growth rate, the real frequency, and the influence of finite beta effects associated with the nonresonant ∇B_0 electron orbit modifications. At large amplitude, allowing only a single mode, it is found that the end of wave growth is due to ion trapping, even when a wide band ($\Delta\omega\sim\gamma$) of the mode occurs, with the growth rate γ comparable to the wave frequency. Contrast with the end of growth by quasilinear diffusion will be given.

Particle Simulation of Instabilities due to Steep Density Gradients. JAE KOO LEE† and C.K. BIRDSALL, U.C. Berkeley*—Instabilities may occur in collisionless Maxwellian magnetized plasmas, driven by the free energy associated with a spatial density gradient. Electrostatic particle simulations were used to study such instabilities with both species magnetized and treated fully nonlinearly. During the linear stage, simulations showed exponential growth in time with the growth rates in fair agreement with a linear nonlocal theory, while the real parts of frequencies were not well resolved in the short growth period. The simulation saturation levels were somewhat above those predicted by existing nonlinear theories. At the time of saturation, the phase space pictures of electrons and ions show bunching in some cases. Clear distinction between drift cyclotron and lower hybrid drift instabilities was not possible; both may have been present.

Field Reversed Ion Ring Stability - Recent Results: Ergodic Orbits and Particle Simulation.* A. FRIEDMAN, U. C. Berkeley, J. DENAVIT, Northwestern Univ., and R. N. SUDAN, Cornell Univ. -- We present new results regarding stability of a field-reversed ion ring in a dense plasma, obtained by numerical simulation using RINGHYBRID, a linearized 3D hybrid code[1]. The ring is moderately thick, with effective aspect ratio of order 4:1, and reversal factor 1.35 on axis. Nonaxisymmetric modes of azimuthal number ℓ are studied. The $\ell=1$ radial mode (precession) is stable, whereas the axial mode (tilt) is unstable. Axial kink modes with $\ell>2$ and radial kink modes with $\ell>3$ are stable, as predicted on the basis of thin-ring theory[2,3].

We have observed effects of ergodic particle orbits in our simulations. In the nonlinear 2D3V zero order behavior the main effect is a loss of left-right symmetry due to the exponential divergence of "neighboring" mirror image trajectories. However, in linearized codes where the perturbation quantities represent displacements between neighboring orbits, the collective behavior can be masked in some cases by rapid single-particle orbit separation.

---

*Supp.by USDOE Contrs. DE-AS03-76SF00034/DE-AT03-76ET53064 and EY76-S-02.2200.

[1] A.Friedman, R.N.Sudan, J.Denavit, Cornell Lab. of Plasma Studies Rept.#268 (1979), submitted to J. Comput. Phys.
[2] R.V.Lovelace, Phys. Fluids 19, 723 (1976).
[3] R.N.Sudan & M.N.Rosenbluth, Phys. Fluids 22, 282 (1979).

DISTRIBUTION LIST

Department of Energy

Hunley, Nelson, Price, Priester, Sadowsky, Siambis

Department of Navy

Condell

Austin Research Associates

Drummond, Moore

Bell Telephone Laboratories

Hasegawa

California State Polytechnical University

Rathman

Columbia University

Chu

Cornell University

Mankofsky

Electrical Power Research Institute

Gough, Scott

General Atomic Company

Helton, Lee

Georgia Institute of Technology

Bateman

Hascom Air Force Base

Rubin

IBM Corporation

Gazdag

JAYCOR

Klein, Tumolillo

Air Force Base

Genoni, Pettus

Los Alamos Scientific Laboratory

Barnes, Burnett, Forslund, Gitomer, Hewett, Lewis, Lindemuth, Lindman, Mason, Neilson, Oliphant, Sgro

Lawrence Berkeley Laboratory

Cooper, Feder, Kaufman, Kunkel, Pyle

Lawrence Livermore Laboratory

Albritton, Anderson, Brengle, Briggs, Bruijnes, Byers, Chambers, Cohen, Condit, Estabrook, Fawley, Finan, Fries, Fuss, Harte, Killeen, Kruer, Langdon, Lasinski, Lee, Maron, Marx, Matsuda, Max, McNamara, Mirin, Nevins, Nielsen, Smith, Tull

Massachusetts Institute of Technology

Berman, Bers, Kulp, Palevsky, Tetreault, Gerver

Mission Research Corporation

Hobbs, Godfrey

NASA - Langley Research Center

Hohl

U.S. Naval Research Laboratory

Boris, Drobot, Haber, Lee, Vomvoridis, Winsor

Northwestern University

Denavit, Crystal

New York University

Grad, Weitzner

Oak Ridge National Laboratory

Dory, Meier, Mook

Princeton Plasma Physics Laboratory

Chen, Cheng, Lee, Okuda, Tang

Princeton University

Graydon

Science Applications, Inc.

McBride, Wagner

Sandia Laboratories

Freeman, Poukey, Quintenz

Stevens Institute

Rosen

Sonoma State University

Johnston

Stanford University

Buneman

University of Arizona

Morse

University of California, Berkeley

Arons, Au-Young, Birdsall,
Buchanan, Chen, Chorin, Friedman,
Grisham, Harned, Hudson, Keith,
Lichtenberg, Lieberman, McKee,
Otani, Potter, Thomas

University of California, Davis

DeGroot, Woo

University of California, Irvine

Pynn

University of California, Los Angeles

Dawson, Decyk , Huff, Liewer,
Lin, Tajima

University of Iowa

Knorr, Nicholson, Joyce

University of Maryland

Guillory, Rowland, Sternlieb,
Winske

University of Texas

Horton, MacMahon

University of Wisconsin

Shohet

Culham Laboratory

Eastwood, Roberts

University of Reading

Hockney

Ecole Polytechnique / Centre de Polytech.

Adam

Bhabha Atomic Research Centre

Aiyer

Gell

Tel-Aviv University

Cuperman

Nagoya University

Kamimura

Max Planck Institute fur Plasmaphysik

Biskamp